DESIGN, ANALYSIS, AND FLUIDIC RECONFIGURATION OF

MULTI-ARM ARCHIMEDEAN SPIRAL FREQUENCY

SELECTIVE SURFACES

A Thesis

by

MICHAEL STEPHEN KELLEY

Submitted to the Office of Graduate and Professional Studies of
Texas A&M University
in partial fulfillment of the requirements for the degree of

MASTER OF SCIENCE

Chair of Committee,	Gregory Huff
Committee Members,	Robert Nevels
	Arum Han
	Jay Porter
Head of Department,	Miroslav Begovic

August 2015

Major Subject: Electrical Engineering

ABSTRACT

Frequency selective surfaces are periodic structures that exhibit a frequency dependent response when interacting with electromagnetic radiation. Several applications include radome design, radar cross section reduction, antenna subreflector design, and minimization of electromagnetic interference. Typical designs have unit cells on the order of half of a wavelength. This size requires practical surfaces to be electrically large, and the unit cell spacing excites unwanted grating lobes. Various reconfiguration mechanisms have been studied in order to increase the dynamic frequency range of the surface. Some common tuning mechanisms include varactors, RF MEMS, and ferrite materials, which are all active designs. Active frequency selective surfaces require additional design considerations for the inclusion of a biasing network and isolation between the DC and RF signals. In some applications spaces, such as electronic warfare and space exploration, active frequency selective surfaces are vulnerable to high energy phenomenon. This work studies various Archimedean spiral frequency selective surface designs, and uses dielectrically tunable fluids as the reconfiguration mechanism.

The unit cell topology of this work is that of a multi-arm Archimedean spiral whose electrical size of the unit cell is smaller than half of a wavelength. Electric field plots of the spiral indicate that the arms of the spiral behave like quarter wave transmission line resonators. Further investigations include dual-band operation, an equivalent circuit model, lattice structure effects, and circular polarization transparency.

These results help to further the understanding of how this class of frequency selective surface operates.

Fluidic reconfiguration offers an alternative tuning mechanism to traditional active designs. Fluidic systems do not require biasing or isolation circuits. The fluidic network in this work consists of a superstrate, comprised of fluidic reservoirs, attached to the copper layer of the dielectrically backed spiral surface. When filled with a dielectric fluid, the surface's effective dielectric constant increases, which decreases the resonant frequency. Doping the fluid with the high dielectric barium-strontium-titanate-oxide particles further increases the effective dielectric constant, and enables tunability using the particle's volume fraction as the independent variable. Simulated and experimental results of various band-stop and band-pass designs are presented and discussed.

ACKNOWLEDGEMENTS

NOMENCLATURE

ABS	Acrylonitrile butadiene styrene
ADS™	Advanced Design Systems ™
AR	Axial ratio
BP	Band-pass
BS	Band-stop
BSTO	Barium-strontium-titanate-oxide
C	Capacitance
c	Speed of light
DC	Direct current
ε_0	Permittivity of free space
ε_r	Dielectric constant
ε_{reff}	Effective dielectric constant
EM	Electromagnetic
ES	Electrical size
f_0	Resonant frequency
FE	Finite element
FSS	Frequency selective surface
GHz	Gigahertz
HFSS™	High frequency structural simulator ™
HRG	Huff Research Group

I	Current
IL	Insertion loss
L	Inductance
MHz	Megahertz
PCPW	Periodic coplanar waveguide
PD	Phase difference
PDMS	Polydimethylsiloxane
PLA	Polylactic acid
PTFE	Polytetrafluoroethylene
R	Resistance
RF	Radio frequency
TE	Transverse electric
TEM	Transverse electromagnetic
TL	Transmission line
TM	Transverse magnetic
μ_0	Vacuum permeability
V	Voltage
v_p	Phase velocity
ω_0	Resonant angular frequency
Z_0	Characteristic impedance

TABLE OF CONTENTS

Page

LIST OF FIGURES

Page

x

LIST OF TABLES

1. INTRODUCTION

With the proliferation of wireless technology in the last century there has been a growing need to study how electromagnetic radiation interacts with matter. Frequency selective surfaces (FSS) are structures that have a frequency dependent response when illuminated by an electromagnetic (EM) wave. These surfaces are repeating structures that are characterized by their period, which is also referred to as the unit cell. Generally, FSSs can be divided into two categories. The first category uses a series of capacitive and inductive layers to create a desired frequency response – much like lumped elements on a breadboard. The second type of FSS is that of a self-resonant structure. This latter type is the FSS class that this work will focus on.

Self-resonant FSSs come in a variety of shapes. Some common examples are linear dipoles, slots, crosses, and rings. These shapes are typically on the order of half of a wavelength. There is interest in reducing the electrical size of the unit cell in order to conserve space, and to increase the frequency at which undesired grating lobes appear. One method for reducing the electrical size of a FSS is to meander the self-resonant shape inside the unit cell. This method increases resonator's self-coupling and lowers the resonant frequency. The design process for meandered structures is that of a simulate-and-tune method with minimal physical connection between the size of the resonator and its center frequency. Spiral type geometries are several times smaller than half of a wavelength, and their center frequency is proportional to their geometry.

For traditional FSSs, after fabrication their frequency response is static. There have been several investigations into expanding versatility of the surface, but the most popular method is adding a reconfiguration mechanism to the surface. Some reconfiguration examples include varactors, RF MEMS, liquid metal FSSs, and ferrite substrates. Active reconfiguration designs are very common. However, adding an active component to the FSS requires additional design considerations. Active designs require biasing networks, and a sufficient level of isolation between the DC and RF signals. In addition, the dynamic range of the chips and their commercial availability are limiting factors when designing the surface. Fluidics offers an alternative option for reconfiguration. Typical applications involve dielectrically loading the system in order to change the device's effective dielectric constant. Fluidic systems do not require any biasing or isolation circuits. In addition, using a tunable fluid opens a continuous range of achievable frequencies as opposed to finite sets that active chips enable.

The research in the proceeding work analyzes and discusses the behavior of multi-arm Archimedean spiral FSSs, and the use of fluidics as a mechanism for reconfiguration. This document is divided into several sections. The next section discusses the background and motivation for this work. This includes discussions on various types of FSSs, different reconfiguration techniques, applications, previous research done in the Huff Research Group (HRG), and electromagnetic fundamentals on FSSs, waveguides, and dielectric material. The third section discusses various multi-arm arm Archimedean spiral designs, their modal frequency responses, incident angle dependence, lattice effects, transmission line resonator behavior, and equivalent circuit

models. The forth section presents measurement techniques and measured results for several multi-arm spiral experiments. The fifth section discusses two dual-band designs through manipulation of the spiral's arm lengths. The sixth section presents and discusses the various fluidic reconfiguration experiments performed using the four-arm spiral designs. The final section concludes this work with a summary of the experimental results, various design challenges that were encountered, and possible future work.

2. BACKGROUND

2.1.   *Common FSS Designs*

A FSS is a periodic structure characterized by the shape within a single repetition. A unit cell is one period of the FSS. Numerical simulations are a popular method for calculating the surface's frequency response. Some of the more common numerical techniques are method of moments, finite element, finite difference time domain, and the spectral domain method – to name a few. The 3-D finite element (FE) electromagnetic software High Frequency Structural Simulator™ (HFSS™) published by Ansys™ will be used to simulate the FSS structures presented in this work [1]. Figure 1 shows some canonical self-resonant FSS shapes seen in literature. Linear dipoles, Figure 1(a), and crosses, Figure 1(b), are some of the simplest and most straightforward designs [2]. Their resonant frequency is proportional to their physical length, which is approximately $\lambda/2$. Figure 1(c) and (d) are other common designs known as the Jerusalem cross and tripole, respectively. These designs are modifications of the basic dipole and cross geometries. Other common shapes are the ring resonator, Figure 1(e), and split ring resonator, Figure 1(f) [3]. Some drawbacks of traditional designs are that they are polarization dependent, and their electrical size excites grating lobes within the frequency band of interest.
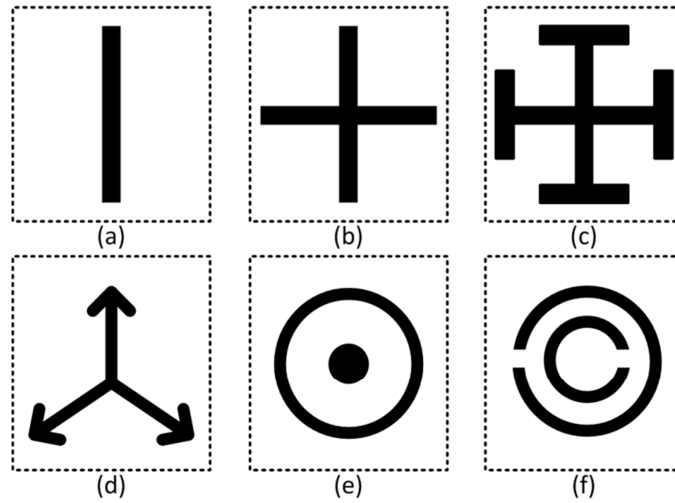
Figure 1 *Some canonical examples of FSS unit cell shapes.*

There is interest in the area of reducing the element size of the FSS to create electrically small structures. This class is commonly referred to as miniaturized FSSs. One reduction method is to create meandered half wavelength dipoles or crosses [4, 5]. The authors in these papers were able to achieve various levels of reduction in electrical size (ES), defined as the resonator's diameter over its free space resonant wavelength, with the smallest ratio being 0.096 for a convoluted cross. Their measured results were in good agreement with their simulated values. However, the authors gave minimal quantitative commentary on how tightly to wrap the dipole in on itself, and the meandering's explicit effect on the resonant frequency. Other authors have further expanded on their work and applied the meandering to more complicated structures [6, 7]. The researchers Sarabandi and Behdad have created layered miniaturized FSSs [8-10]. The work in [9] achieved a minimization ratio of 0.0769. However, the center frequency of all of these structures exhibits a dependence on the incident angle of the

5

incident plane wave. These aforementioned designs offer a method to decrease the unit cell size, but there is very little in the way of a design method for targeting a desired frequency band.

2.2.   *Spiral FSSs*

Spirals are useful because they exhibit electrically small behavior while being mathematically defined, but they are not as popular as the previous designs. A common use for spirals in the RF field is that of a radiator in an antenna [11-13]. In contrast to self-resonant FSSs, these are active structures often operated in a travelling wave configuration. For a standalone spiral FSSs the surface is passive, and the elements operate in a self-resonant mode at a lower frequency than their traveling wave counterparts. Several researchers have investigated different spiral FSS topologies [14-17]. Their work leans towards the experimental side with a minimal physical insight into designing the FSS past the simulate-and-tune method.

The authors in [14] ran multiple simulations investigating various meandered structures. The purpose of their work was to illustrate how meandering decreases the unit cell size, and which geometry was the smallest. Through their iterative investigation they found that the four-arm rectangular spiral had the smallest electrical size out of all the proposed geometries. However, they didn't link any of the square spiral's design features to its center frequency. This paper was more of an observation of how meandering a cross structure lowers the center frequency and decreases its electrical footprint.

In [15] the authors use multi-arm logarithmic and linear spirals to create several different FSS designs. They state that the arms of the spiral are about quarter wavelength long, but they don't elaborate beyond this. The paper states the experimental results of various FSS design iterations. One of their goals was to create orthogonal polarizations by having left handed and right handed neighboring two-arm spirals populate the surface. Their results indicated that the handedness of the spiral did not create an orthogonal polarization. Another design iteration had the neighboring spirals rotated 90° from each other, which yielded a weak orthogonal polarization. The last design they investigated was a four-arm linear slot spiral. Their findings show that this surface yields a band-pass response. This paper was an experimental proof-of-concept investigation into several spiral designs iterations where they elaborated on which designs exhibited the desired behavior and which designs did not.

In [16] the authors investigate multiple configurations of a single arm Archimedean spiral FSS. They go on to experimentally test the surface for different slant angles, i.e. the angle in which the spiral was tilted compared to the polarization axis of the reference antenna. Their results indicate that the slant angle changes the polarization vector of the incident wave. This conclusion is similar to the meandered polarizer FSS results in [18]. Their initial hypothesis was that there would be a single resonance over the measured band, 2 to 18 GHz, but they saw multiple resonant dips. They conjectured that the spiral operated similar to the split ring resonators listed in [3]. Based on their observations they concluded that the first resonant frequency was proportional to the spiral's length, but they could only speculate as to the mechanism for the other

7

resonances. Overall, they observed a polarization shift caused by the surface, but offered little in the way of a design methodology. Another group made slot version of this FSS [17], but in the infrared frequency range. Their theoretical part borrowed heavily from [16]. This latter work didn't build on any design methodology, but rather built a slot spiral in the infrared band.

2.3. *Frequency Selective Surface Basics*

A good general resource for FSSs is chapter 16 in [19], and an excellent resource for understanding Floquet analysis of periodic arrays is [20]. The proper basis functions to describe the fields of the FSS are derived from a Floquet series, which is a periodic Fourier series. A one dimensional Floquet series takes the form

$$h(x) = \frac{2\pi}{a} \sum_{n=-\infty}^{\infty} \tilde{f}\left(\frac{2n\pi}{a}\right) e^{-j\frac{(2n\pi+\varphi)x}{a}} \tag{1}$$

where *h(x)* is a periodic function, *a* is the length of the period, φ is a real constant, *n* is the periodic index, and *f-tilde* is the Fourier transform of the complex function *f(x)*. Setting $\varphi = 0$ turns (1) into a Fourier series [20]. For periodic surfaces the eigenfunctions of the electric field are the transverse electric (TE) and transverse magnetic (TM) modes. Transverse means that the field component in the direction of propagation is zero, e.g. a TE_z wave means that $E_z = 0$. The subscript denotes the transverse direction. For the rest of this work the direction of propagation is the z-direction, and the subscript will be dropped from the notation because it is implied. Using the periodic nature of the surface the electric field takes the form

$$\vec{E}^{TE}(x,y,z) = \sum_{m,n=-\infty}^{\infty} \vec{E}_{mn}^{TE}(x,y)e^{-l+jk_{zmn}z} \tag{2}$$

$$\vec{E}_{mn}^{TE}(x,y) = \frac{\hat{x}k_{ymn} - \hat{y}k_{xm}}{\sqrt{D_x D_y \left(k^2 - k_{zmn}^2\right)}} e^{-j\left(k_{xmn}x + k_{ymn}y\right)} \tag{3}$$

where $\vec{E}_{mn}^{TE}(x,y)$ is the normalized electric field over the unit cell. For the TM mode the

k_{ymn} and k_{xm} variables switch places. The propagation constants of the system are defined

by the lattice geometry and incident angle of the incoming plane wave.

$$k_z = \sqrt{k_0^2 - \left(k_{xm}^2 + k_{ymn}^2\right)} \tag{4}$$

$$k_{xm} = \frac{2\pi m}{D_x} + k_0 \sin\theta_{inc} \cos\varphi_{inc} \tag{5}$$

$$k_{ymn} = \frac{2\pi n}{D_y} - \frac{2\pi m}{D_x}\cot\Omega + k_0 \sin\theta_{inc} \cos\varphi_{inc} \tag{6}$$

$$k_0^2 = \omega_0^2 \varepsilon\mu \tag{7}$$

The variables D_x and D_y are the unit cell sizes in the x and y directions respectively, and

Ω is the slant angle between the unit cells. Figure 2 illustrates the geometry of a slot

dipole FSS in a triangular lattice with a slant angle of Ω. The incident field is a plane

wave coming from a direction of θ_{inc} and φ_{inc} in a spherical coordinate system. The

eigenvectors are the TE_{mn} and TM_{mn} polarizations. The summation of these two modes

equals the total fields excited on the surface, e.g.

$$\vec{E} = \vec{E}_{TE} + \vec{E}_{TM}. \tag{8}$$

When creating a FE model the propagating modes are the ones of interest, and if the

observation point is far enough away the evanescent modes are neglected from analysis.

9

Generally, the propagating modes are preferred to be the TE_{00} and TM_{00} modes with all other modes designed to be evanescent.
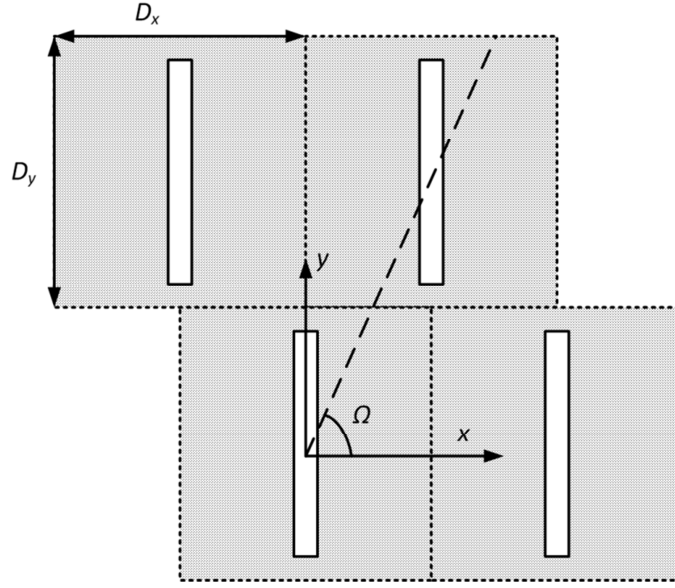
***Figure 2** An array of dipole slots in a triangular lattice with a slant angle of Ω.*

One design consideration of arrays is that of grating lobes. Grating lobes are peaks with equal amplitude that arise due to constructive and destructive interference due to the array's lattice structure. Their cutoff frequency is

$$f_c = \frac{v_p \csc(\Omega)}{D(\sin(\theta_{inc})+1)} \quad \text{Hz} \tag{9}$$

with v_p being the speed of light in the medium, D being the unit cell size of the FSS, and θ_{inc} is the incident angle of the plane wave. If $D_x \neq D_y$ then both permutations need to be calculated in (9). Other formulas for various FSS lattices are listed in [21]. Ideally the designer wants to choose a FSS lattice and size so that the first grating lobe appears

10

outside of the band of interest. Unit cells sizes on the order of half of a wavelength produce grating lobes in the frequency band of interest. Small element sizes allow for close packing, which increases the cutoff frequency for the grating lobes.

2.4. *Reconfigurable FSSs*

Adding a reconfiguration mechanism to a FSS expands its versatility, but it also adds additional design constraints. A common method for reconfiguration is to add a varactor diode to the surface [22-26]. These designs incorporate the varactors at various points to capacitively load the FSS. The biasing voltage controls the operating band of the surface. Adding a varactor requires additional design considerations due to the presence of a biasing and isolation circuits. Other reconfigurable designs have used RF MEMS [27], ferrite substrates [28], and passive LC components [29, 30]. For active designs the commercial availability and biasing ranges puts a limiting factor on the achievable frequency bands.

Fluidic reconfiguration provides an alternative to RF chip designs where active devices would not ideal, such as electronic warfare and space exploration. One reconfiguration method is to use plugs of liquid metal as the variable loading mechanism [31-33]. In [31] the authors create a resonant dipole grid by filling a lattice of polytetrafluoroethylene (PTFE) tubes with plugs of Mercury separated by mineral oil. Varying the metal plug's length makes the surface resonant at different frequencies. The designs in [32, 33] illustrate two different tuning configurations for the liquid metal. The first configuration, similar to [31], fills the channels with liquid metal plugs separated by

11

mineral oil. These plugs capacitively couple to the patch layer changing the effective capacitance. The second configuration involves completely filling the tubing with liquid metal thus creating an inductive loop that changes the effective inductance. These latter authors' results show a tunable frequency range across the X-band.

The last paper of note is a short letter detailing the use of fluid filled substrates as the tuning mechanism [34]. In this letter the authors put paraffin wax inside a hollow acrylonitrile butadiene styrene (ABS) substrate. The addition of the wax shifted the resonant frequency down by 2.7 GHz to just above 14 GHz. The original center frequency was around 16.5 GHz, but this is an estimated value based on graphical data. In the conclusions the authors comment on how other frequency bands are available if other low loss materials are used. This paper was a one shot proof-of-concept illustration on how fluids can be used to change the resonant frequency of a FSS.

2.5.   *Applications of FSSs*

FSSs have been incorporated into various application spaces. Some of the common applications include radome design, radar cross section reduction, Cassegrain subreflectors design, and RF lenses [35-37]. For radome design and other stealth technologies the attractive property of the FSS is that it lets certain frequencies through while reflecting others. For example, the nosecone of a stealth aircraft could be a FSS. The plane's antenna operates in the pass-band of the FSS, and the enemy's radar operates in the stop-band. Thus the cone would be transparent to the plane's antenna in the pass-band while in the stop-band the enemy's radar would be reflected at an angle

away from the enemy's receiver [2]. This adds more versatility to the structure and allows for an internal antenna versus placing the antenna outside traditional stealth material. With wireless technology becoming ubiquitous FSSs have found their way into building design [38-41]. In these applications the FSS isolates separate Wi-Fi networks, suppresses cellphone signals, and other proprietary wireless transmissions. For Cassegrain subreflectors the FSS acts as the antenna's subreflector. The design goal is to have the surface reflective in one band while transparent in another. This enables multiple configurations for the antenna. NASA's Cassini space probe's antenna uses a FSS for its reflector. Various other antenna and FSS topologies have been studied [42-44]. The general design procedure is to build the antenna and FSS separately, and then measure the performance of the combined system.

2.6.   *Previous Work in the HRG*

One of the previous Masters students from the HRG group, Elizabeth Wells, worked to create a fluidically reconfigurable spiral band-stop FSS [45]. Figure 3 shows the spiral design that she used. This is called a cross spiral. Figure 4 shows the spiral's frequency response versus θ_{inc}. The resonant frequency of the spiral is dependent on θ_{inc}, which makes the incident angle a constraining variable. The cross spiral is a viable FSS design, but care need to be taken in its application due to the angular dependence.

She performed several reconfiguration experiments. The first experiment placed polydimethylsiloxane (PDMS) discs doped with barium strontium titanate-oxide particles (BSTO) on top of the spirals. This was a static reconfiguration experiment.

Figure 5 shows the experimental setup. Measurements show that as the volume fraction of BSTO particles increases the resonant frequency decreases. One of the design challenges of this setup is the proper placement of the discs on the surface. If the discs are improperly aligned then the capacitance of the unit cells across the surface is no longer uniform. The net effect of this displacement is the creation of a second resonance, which will either widen the initial stop-band or create a separate stop-band. Both cases diminish the bandwidth and suppression level of the stop-band. Figure 6's curves show the effects of this misalignment.
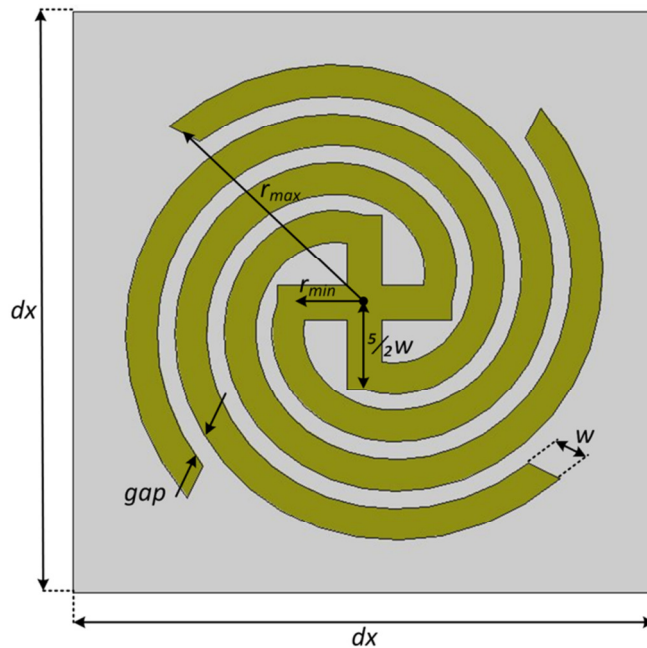
Figure 3 *The cross spiral design from [45].*
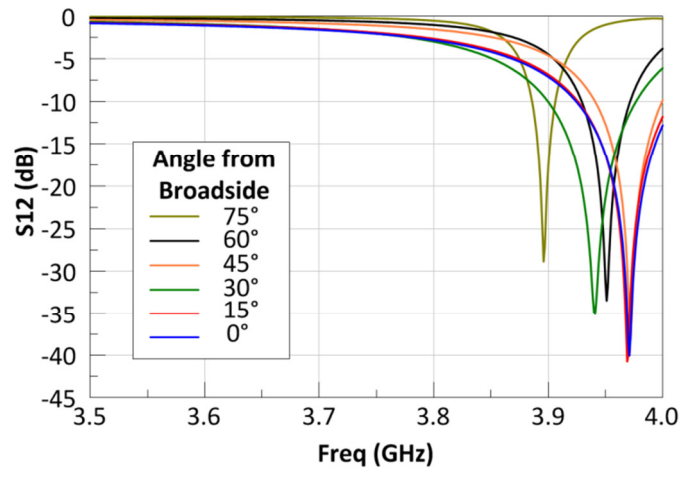
Figure 4 *Simulations show an angular dependence in the cross spiral's frequency response versus θ*$_{inc}$ *[45].*
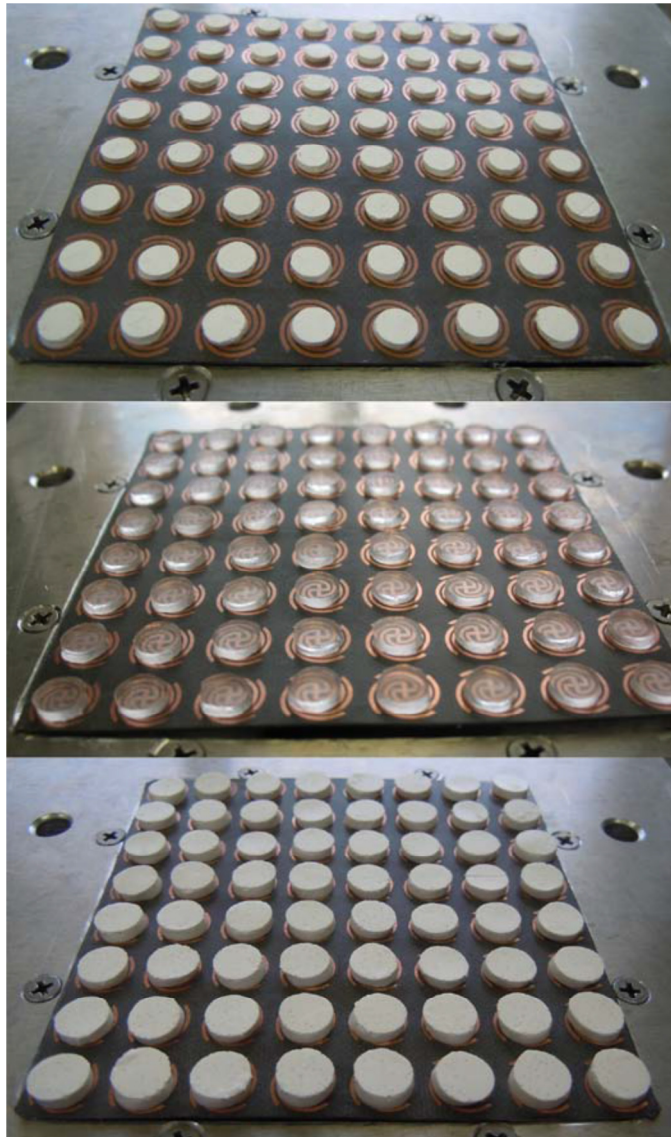
Figure 5 *The static tuning experiment using BSTO doped PDMS discs. The top picture displays discs with a 40% volume fraction, the middle picture's disc have a 0% volume fraction, and the bottom picture shows discs with a 25% volume fraction [45].*

The second set of experiments involved the creation of a stratified channel

structure, pictured in Figure 7, in which fluidic dispersions flow through a channel layer,

and then up into the reservoir above the spiral traces. This changed the superstrate's

effective dielectric constant, and lowered the resonant frequency. The channel structures

16

were made of PDMS and plasma bonded to the FSS. Only the center 16 spirals had reservoirs above them. The other spirals were covered by solid PDMS. The base fluid was silicone oil doped with BSTO. When the channels were filled with non-doped silicone oil the center of the stop-band was at 3.1 GHz versus the unloaded center frequency of 3.91 GHz. When a 10% BSTO dispersion loads the reservoirs the frequency response becomes bimodal with a second resonance around 3 GHz. However, when the volume fraction was increased to 20% there was a rupture between the channel layers due to an increase in internal pressure caused by an in increase in viscosity. At higher volume fraction the dispersion has a consistency similar to a paste. Figure 8 illustrates the rupture between the channel layers. A second iteration of the experiment was created, but the bonding failed during a repeat of the 10% volume fraction experiment. Ms. Wells suggests future iterations use different materials to create a more mechanically stable structure. In addition to the structural failures this design had significant losses for higher volume fractions. A consequence of increased losses is that several of the experimental results had a stop-band with insufficient suppression, e.g. suppression less than -10 dB, which made the surface unusable as a band-stop filter.
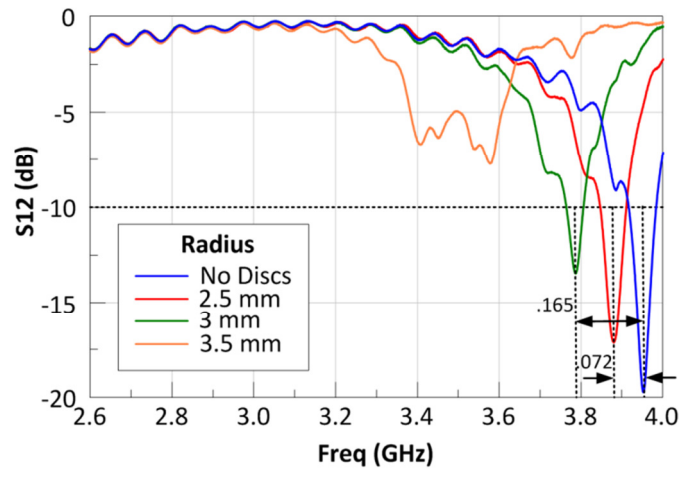
Figure 6 *Results from inaccurately placed PDMS discs [45].*
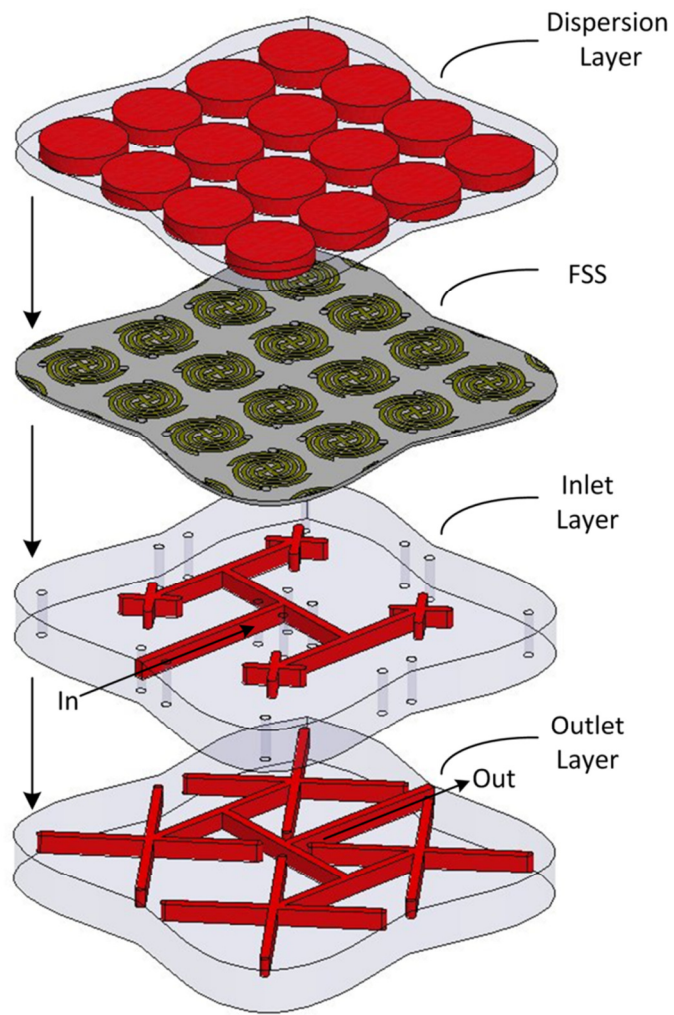
Figure 7 *An expanded view of the stratified surface used in the fluidic dispersion experiments in [45].*

Figure 8 *The internal pressure created by the fluids caused the channel bonding to fail [45].*

Ms. Wells' work demonstrated a different topology for a spiral FSS, and how it can be tuned using fluidic dispersions. Her work illustrated several design challenges. Alignment of the materials plays an important role in determining the center frequency of the surface. The materials were a significant limiting factor in the design. The losses had to be small or else the stop-band's suppression would diminish to an unusable level. The use of plasma bonding created issues because it didn't form a strong enough bond between the channel layers. The last point of note is that there was little in the way of a design methodology or analysis of the spiral's field structure that would enable an independent designer to create a spiral in a different frequency band. The work that Ms. Wells did was a good proof of concept, and it highlighted several design challenges, but more analytical work and design investigation needs to be performed.

2.7.   *Waveguide Fundamentals*

Waveguides are a class of transmission lines typically used in the microwave region of the EM spectrum. The most common waveguide designs are hollow rectangular or circular metal enclosures with an EM wave propagating from one open end to the other. Figure 9 shows a schematic for a standard rectangular waveguide with inner dimensions *a* and *b*. Waveguides are typically excited by a coaxial probe. The modes inside a waveguide are TE or TM, but they have a different field distribution than their Floquet counterparts. For waveguides, the Helmholtz wave equation takes the form

$$\left(\frac{\partial^2}{\partial x^2} + \frac{\partial^2}{\partial y^2} + \frac{\partial^2}{\partial z^2} + k^2 \right) H_z = 0 \tag{10}$$

for TE modes and

$$\left(\frac{\partial^2}{\partial x^2} + \frac{\partial^2}{\partial y^2} + \frac{\partial^2}{\partial z^2} + k^2 \right) E_z = 0 \tag{11}$$

for TM modes. The cut off wave number is the same for both modes and takes the form

$$k_c = \sqrt{k_x^2 + k_y^2} = \sqrt{\left(\frac{m\pi}{a} \right)^2 + \left(\frac{n\pi}{b} \right)^2} \qquad \begin{cases} m = 1,2,3... \\ n = 0,1,2,3... \end{cases} \tag{12}$$

with *m* and *n* being the modal indices. However, the TM mode's indices are never equal to zero because of the boundary conditions at the walls. The wave number and propagation constant are

$$k^2 = \omega^2 \varepsilon \mu_0 \tag{13}$$

$$k_z = \sqrt{k^2 - k_c^2}. \tag{14}$$

The cutoff frequencies for the modes are

$$f_c = \frac{1}{2\pi\sqrt{\varepsilon\mu_0}}\sqrt{\left(\frac{m\pi}{a}\right)^2 + \left(\frac{n\pi}{b}\right)^2}. \tag{15}$$

Below the cutoff frequency the modes are evanescent and exponentially decay. Solving the wave equation produces the vector potential

$$\Psi^{TE} = A_{mn}\cos\left(\frac{k_{x,mn}\pi x}{a}\right)\cos\left(\frac{k_{y,mn}\pi y}{b}\right)e^{-jk_z z} \tag{16}$$

for TE modes. A_{mn} is an arbitrary constant determined by the excitation. For TM modes the cosines change to sines. The preferred mode of operation for a rectangular waveguide is the TE_{10} mode. There are TM waveguides, but the waveguide used for measurements in this work is a TE type. For the rest of this work, this is the implied mode, and as such the analysis will be limited to the TE_{10} mode of the waveguide. The electric and magnetic fields for the TE_{10} mode are

$$E_x = E_z = H_y = 0 \tag{17}$$

$$E_y = \frac{-j\omega\mu a}{\pi}A_{10}\sin\left(\frac{\pi x}{a}\right)e^{-jk_z z} \tag{18}$$

$$H_x = \frac{jk_z a}{\pi}A_{10}\sin\left(\frac{\pi x}{a}\right)e^{-jk_z z}. \tag{19}$$

$$H_z = A_{10}\cos\left(\frac{\pi x}{a}\right)e^{-jk_z z} \tag{20}$$
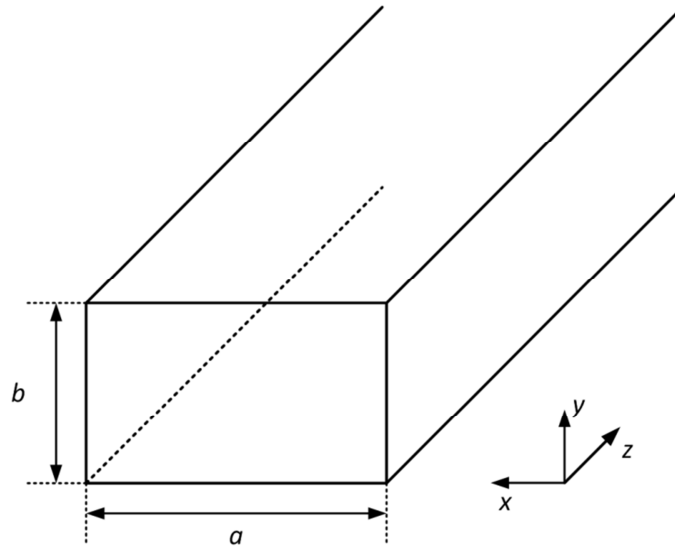
Figure 9 *A schematic outline of a rectangular waveguide*

An alternative formulation of waveguide modes is that of bouncing plane waves. The sinusoidal formulation of the waveguide's fields can be broken into complex exponentials.

$$\sin(x) = \frac{e^{jx} - e^{-jx}}{2j} \tag{21}$$

The physical interpretation of this is that of two plane waves are reflecting off of opposite walls at angle θ_{inc}. Chapter 9 in [46] has an excellent section that explains the reflection model of waveguide propagation. What makes this reference superior to other texts is that it derives the fields for this model. The equivalent incident angle of the reflected wave is calculated using the reflection model

$$\cos(\theta_B) = \frac{k_c}{k} \tag{22}$$

23

$$\theta_{inc} = 90° - \cos^{-1}\left(\frac{k_c}{k}\right). \tag{23}$$

Sticking (12) and (13) into (23) shows that the incident angle is a function of the waveguide's cross sectional dimensions and frequency of operation.

A physical consequence of TE and TM waveguide modes is that they are dispersive. This is in contrast to plane wave propagation with TEM polarization, which is non-dispersive. Any object being measured inside the waveguide with an angular dependence will be dependent on frequency due to the dispersive nature of waveguides.
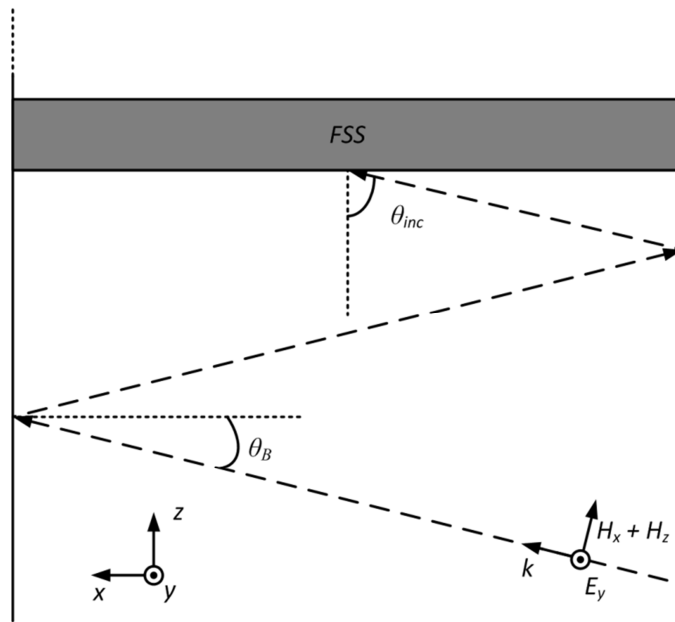
Figure 10 A vector diagram of the reflection model of waveguide propagation for the TE$_{10}$ mode.

2.8.   *Dielectrics and Electromagnetic Mixing Rules*

Dielectric material is an electrical insulator that can be polarized by an applied electric field. The electrons inside a dielectric are tightly bound to their nucleus, and are

not free to flow. However, an applied electric field induces a torque on the dielectric's charges, i.e. dipole moment, until they are aligned with the applied field. This polarizes the material, and increases the energy stored in the electric field. One way to encapsulate this behavior is through a property known as permittivity ε defined by

$$\varepsilon = \varepsilon' - je'' \tag{24}$$

$$\varepsilon' = \varepsilon_r \varepsilon_0 \tag{25}$$

$$\tan \delta = \frac{\varepsilon''}{\varepsilon'}. \tag{26}$$

Equation (26) is known as the loss tangent, and is a function of the losses in the dielectric material. Some examples of losses are charge carrier mobility and energy loss due to the dipole moment relaxation. Analogous to a perfect electric conductor, a perfect dielectric would have no losses. When defining a dielectric's properties the relative permittivity, i.e. the dielectric constant ε_r, and the loss tangent are required.

Fluids can also be electrical insulators. Some common non-conducting fluids are mineral oil, Fluorinert™, and silicone oil. Their dielectric constants are typically between 2 and 3. The dielectric constant of the fluid can be changed by mixing in dielectric particles. A common formula for calculating the effective dielectric constant of a mixture is the Clausius-Mossotti formula. This formula contains variables determined by various microscopic attributes such as polarizabilities and scatterer densities [47]. For macroscopic engineering these variables are not the most convenient. Another mixing formula is the Maxwell Garnett mixing rule.

$$\varepsilon_{reff} = \varepsilon'_e - j\varepsilon''_e + 3f\left(\varepsilon_e - j\varepsilon''_e\right)\frac{\varepsilon'_i - \varepsilon'_e - j\left(\varepsilon''_i - \varepsilon''_e\right)}{\left(1-f\right)\varepsilon'_i + \left(2+f\right)\varepsilon'_e - j\left[\left(1-f\right)e''_i + \left(2+f\right)\varepsilon''_e\right]} \quad (27)$$

The variables ε_e and ε_i represent the dielectric constants of the background fluid and

dielectric particles, respectively, with the primes indicating the real and imaginary parts.

The variable f is the volume fraction of the particles to the background fluid. The

particles are assumed to be spherical. For other particle geometries, e.g. needles, the

formula needs to be modified, but because the particles in this work are spherical further

discussion is beyond the scope of this work.

3. MULTI-ARM ARCHIMEDEAN SPIRAL DESIGNS

3.1. *Metal Spiral Design*

One use for spirals in the RF field is that of its use as a radiator in an antenna [11-13, 48]. Spiral antennas have multiple operational modes, but are most commonly center fed through a multi-port feed network, and operated in one of its traveling wave modes. A multi-arm spiral can be operated in a resonant mode at a lower frequency than its traveling wave counterpart. This is accomplished by shorting the arms together in the middle, and viewing each arm as a quarter wave resonator. The geometry for this work is that of a multi-arm Archimedean spiral. The four-arm Archimedean spiral has several favorable attributes, and will the canonical example used throughout this work. The band of interest is the IEEE S-band, which is 2 to 4 GHz. Figure 11(a) depicts a four-arm copper spiral, which is referred to as a *metal spiral*. It has a band-stop frequency response. The design parameters are the arm width w, gaps spacing s, number of turns of the spiral N_t, number of arms n, copper thickness t, and unit cell size D. The four-arm designs parameters are $w = 0.6$ mm, $s = 0.408$, $D = 9.95$ mm, $t = 70$ µm, and $N_t = 1.03$. The first grating lobe appears at 15.08 GHz at $\theta_{inc} = 34°$, which is outside the frequency band of interest.
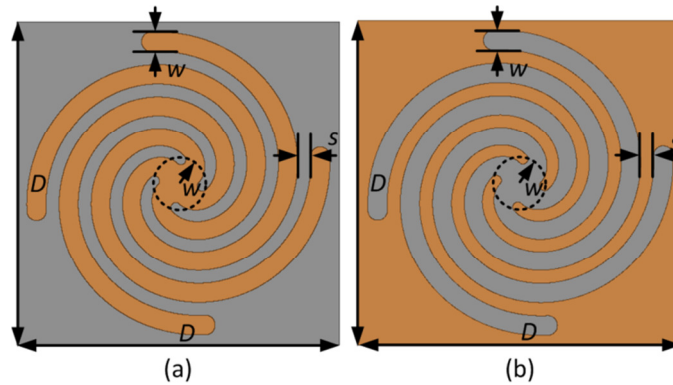
Figure 11 *The geometry of the metal (a) and slot (b) spirals.*

3.2. ***The Slot Spiral: A Complementary Structure***

Switching the metal and non-metal section creates a design with a band-pass frequency response. This geometry is called a *slot spiral*. The metal spiral and slot spiral are duals of each other. Figure 11(b) shows the geometry of the slot spiral. The design parameters for both structures are the same with the exception of $t = 35$ μm.

Figure 12 shows the results for both spirals when there is no substrate and the conductor is defined as perfect electric conducting (PEC) sheet. The frequency responses of the metal and slot spiral are complementary. The standards for this claim are that the 3 dB points and center frequency are exactly the same. However, Figure 13 shows that with a 62 mil Duroid™ 5880 substrate, finite metal thickness, and the conductor being made of copper the two frequency responses are no long complementary. Babinet's principle states three requirements for complementary structures: planar, perfectly conducting, and infinitely thin [49]. Adding a finite copper thickness to the model breaks these last two conditions. In addition, adding a dielectric adds another asymmetry to the design, and shifts the center frequency down from 4.8 GHz to 3.91 GHz for the metal

28

spiral and 3.84 GHz for the slot spiral. Application of Babinet's principle switches the

electric and magnetic fields for complementary structures. For example, a y-directed

electric field and an x-directed magnetic field for become an x-directed electric field and

a y-directed magnetic field. Having a dielectric material only on one side of the surface

will not affect the electric field equally for both designs.
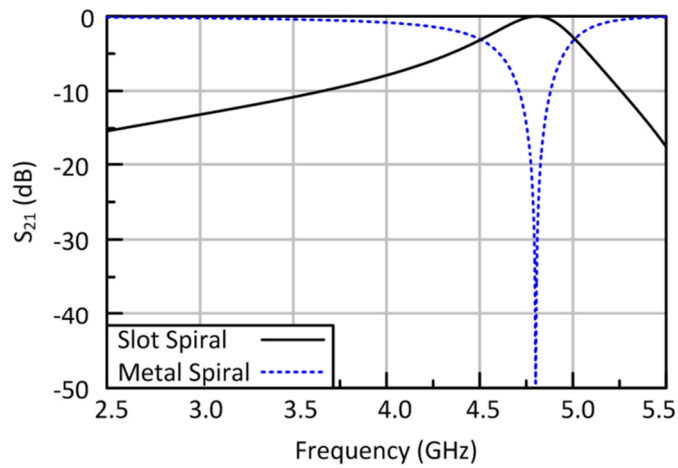
Figure 12 *The metal and slot spirals have perfect complementary responses when there is no dielectric and the conductors are PEC sheets.*
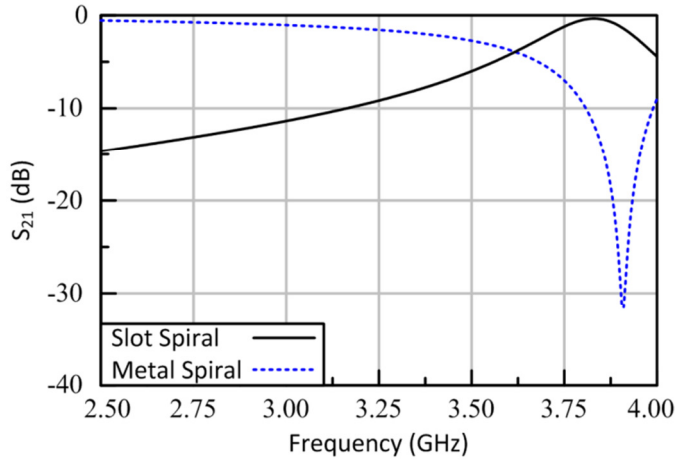
Figure 13 *The complementary nature of the two spirals is broken when adding a dielectric and a finite metal thickness.*

3.3. *Quarter Wavelength Transmission Line Resonator Behavior*

Figure 14 is a plot of the time average electric field of the four-arm metal spiral. This plot reveals several structural properties of the spiral FSS. The electric field of the spiral has a maximum at the ends of the arms and a minimum in the middle. This indicates that each arm behaves similar to a quarter wave resonator. In between the arms the electric field alternates between positive and negative, which is indicative of a periodic coplanar waveguide (PCPW) transmission line [50]. Figure 15 is a cross sectional view in the y-z plane of the spiral's unit cell, and displays the vector electric field pattern. The vector pattern is consistent with the quasi-TEM even mode for a periodic coplanar transmission line. These two structural behaviors indicate that the arms of the FSS operate similar to PCPW transmission line resonators. The center frequency of the metal spiral is 3.91 GHz, which corresponds to an electrical length slightly longer than the $\lambda_g/4$ calculated by just using the physical length of the arms. For the slot spiral,

30

the surface current density is the analogue of the electric field. Figure 16 shows the time average current density for the four-arm slot spiral. The current distribution also shows PCPW transmission line resonator behavior as well. Figure 17 is the electric vector field plot of the four-arm slot spiral in the y-z plane. The field distribution indicates that the slot spiral operates in a quasi-TEM even mode.
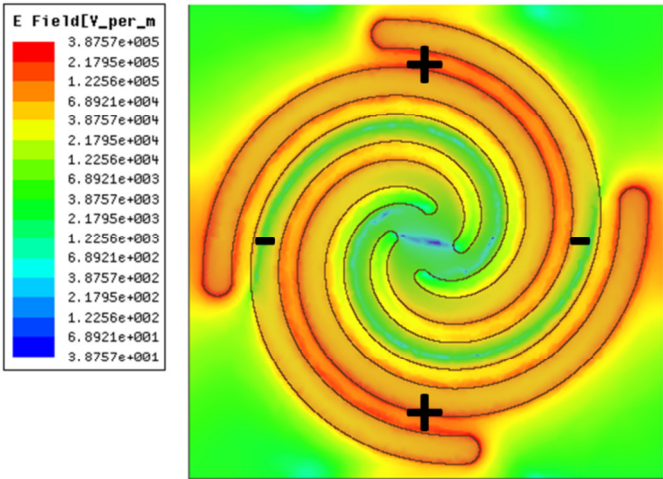
Figure 14 *The time average electric field distribution of the four-arm metal spiral.*
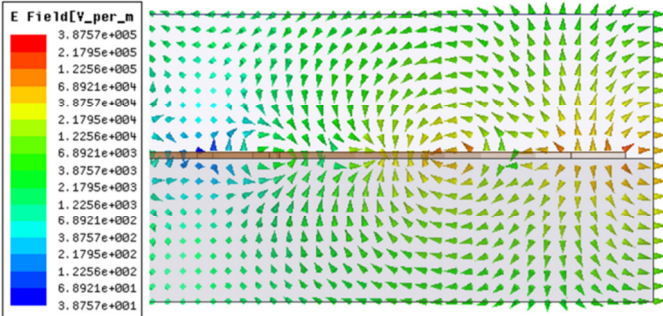
Figure 15 *The electric vector field plot of the right half of the metal spiral in the y-z plane.*
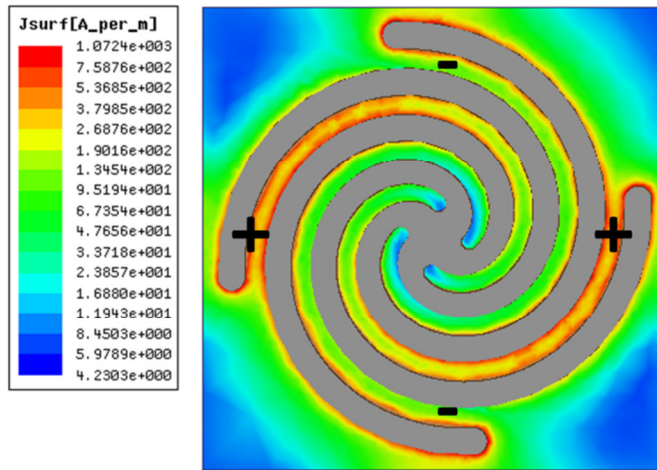
Figure 16 *The time average surface current density for the four-arm slot spiral.*
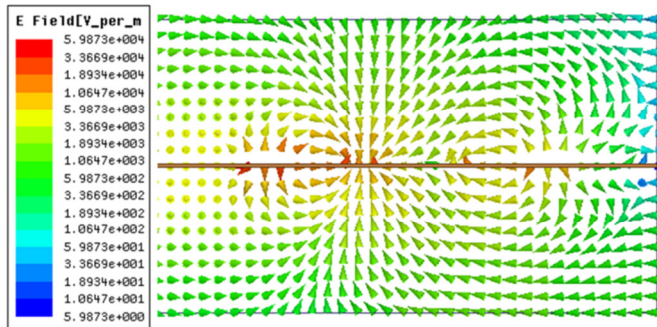
Figure 17 *The electric vector field plot of the right half of the four-arm slot spiral in the y-z plane.*

Transmission line resonators tend to be electrically longer than their physical

length [51, 52]. The center frequency of the spiral is a function of several effects. The

largest determining factor is the arm's physical length. The next highest order effects are

the mutual coupling between cells, fringing fields at the ends of the arms, and additional

self-inductance caused by the copper's thickness. One method for modeling these effects

is to treat them as length extensions and subtractions [52, 53]. Their sum total is equal to a quarter wavelength,

$$\lambda_g = 4\left(L_{\text{physical}} + \Delta L_{\text{coupling}} + \Delta L_{\text{fringing fields}} + \Delta L_{\text{self-inductance}}\right). \tag{28}$$

The coupling and fringing fields are capacitive in nature for the metal spiral (inductive for the slot spiral), and are treated as length extensions. A thicker copper layer results in an increase in the self-inductance of the surface, which behaves like a length subtraction. Using the spiral's physical length is a good first order approximation for calculating the resonant frequency.

Figure 18 shows the simulated values for the four-arm designs. The unit cell size was swept to show the effect that coupling has on the center frequency. As the unit cell becomes larger the center frequency approaches an asymptotic value. At a nearest neighbor distance of about $0.1\lambda_0$ the asymptotic value is reached for the four-arm design. This indicates that at certain point the nearest neighboring resonator minimally affects the center frequency. However, Figure 19 shows that as the nearest neighbor spacing increases the quality factor increases – with the quality factor being defined as the resonant frequency over the 3 dB bandwidth. This increase continues past the $0.1\lambda_0$ limit for the center frequency indicating that the 3 dB bandwidth decreases the larger the unit cell size.
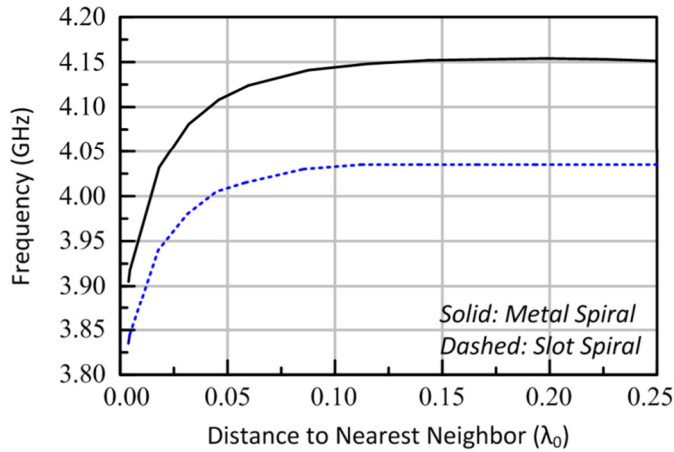
Figure 18 The simulated center frequencies for the four-arm designs plotted versus their unit cell size.
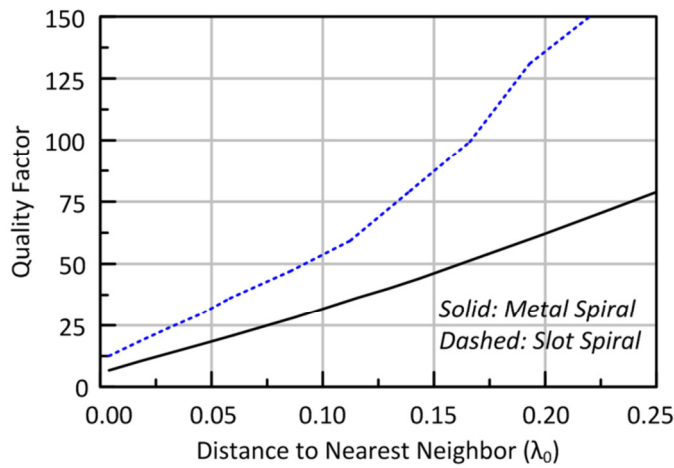
Figure 19 The quality factor of the four-arm spirals plotted versus their unit cell size.

Figures 20 and 21 illustrate that as the arm width and gap spacing for the metal spiral increases the fractional bandwidth decreases. For these simulations the unit cell size was increased, but the nearest neighbor distance was kept at 2.00 mm in order to minimize any change in nearest neighbor coupling. For Figure 20 the gap spacing was set to $s = 0.3$ mm; for Figure 21 the arm width was kept constant at $w = 0.3$ mm. The

variable N_t was tuned so the center frequency was near 3.9 GHz for all simulations in order to offer a quantitative comparison. To minimize the self-inductance term, the spiral was defined as a PEC sheet. The independent variable is

$$\chi = \frac{w}{w + 2s} \tag{29}$$

which is a design variable for PCPW outlined in [50]. The general trends are that as the arm width becomes larger the quality factor decreases. When the gap spacing decreases, χ becomes larger. As the gap spacing becomes smaller the quality factor increases.
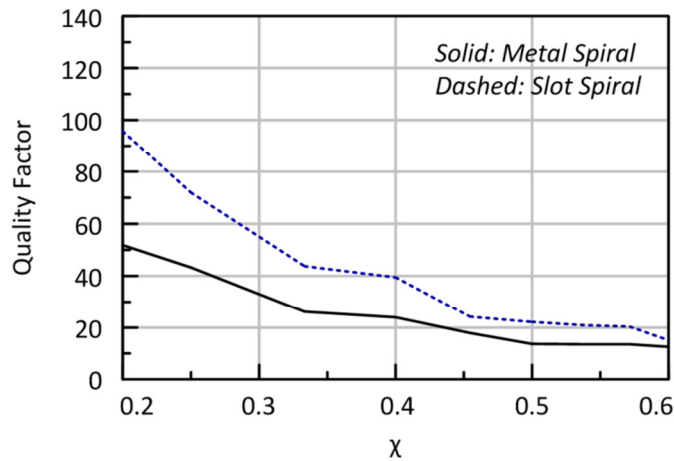
Figure 20 *The quality factor of the resonator versus the parameter χ as the design parameter w increases.*
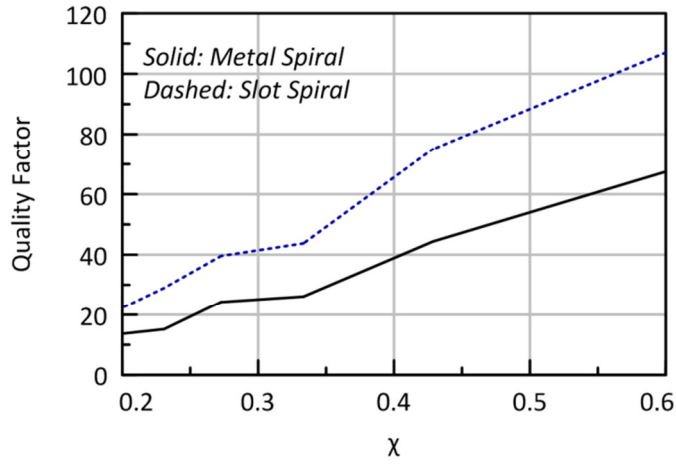
Figure 21 *The quality factor of the resonator versus the parameter χ as the design parameter s increases. The parameter χ is inversely related to s.*

Figure 22 shows the simulated resonant frequency of the four-arm spiral designs as a function of copper thickness. Simulations indicate that the center frequency and the copper thickness are linearly related. The increase in copper thickness increases the self-inductance of the resonator and increases the resonant frequency. The increase in self-inductance behaves like an equivalent length subtraction for both metal and slot spirals.
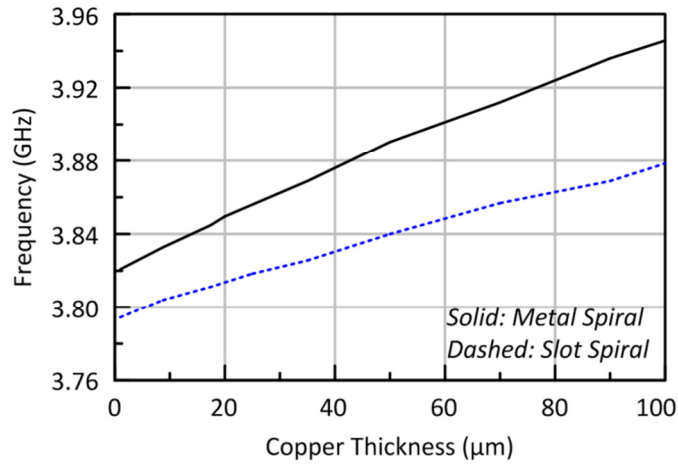
Figure 22 *The resonant frequency of the four-arm spirals as a function of copper thickness.*

3.4. *Floquet Modes and Incident Angle Dependence*

When creating a FE simulation using Floquet analysis care needs to be taken

with the propagating and evanescent modes [1]. All of the propagating modes need to be

included. The port distance from the surface has to be large enough so that the

evanescent modes are attenuated enough to be neglected from the analysis. For $D = 9.95$

mm the next highest order mode, the $TE_{0\text{-}1}$ mode, has attenuation constant of 4.72 dB.

The distance from port 1 to port 2 is 25 mm. This mode is attenuated by 59 dB by the

time it reaches port 2, and it can be ignored from the simulation. The two propagating

modes for the designs in this work are the TE_{00} and TM_{00} modes. Figure 23 shows the

frequency response of these modes at normal incidence for the four-arm spiral. They're

identical.
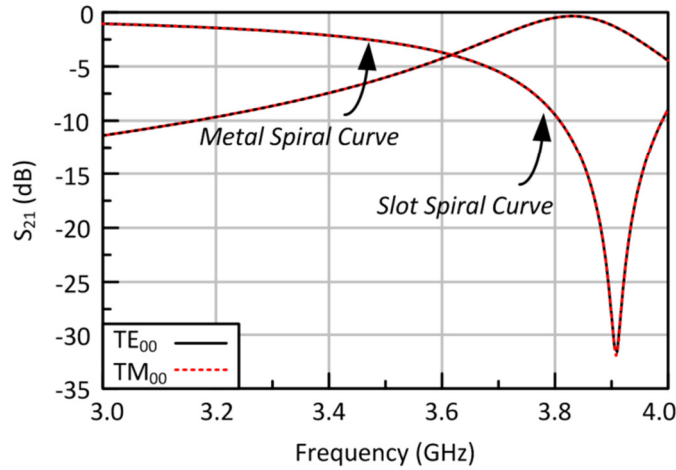
Figure 23 *The TE$_{00}$ and TM$_{00}$ modes for the metal and slot spirals have identical frequency responses.*

Figure 24 shows the simulated results for the metal and slot spiral versus φ_{inc}. There are multiple curves in the plot, but they lie on top of each other. These simulations show that the four-arm metal and slot spirals frequency response is invariant under a φ_{inc} rotation. Traditional designs, e.g. resonant dipoles and crosses, are dependent on φ_{inc}, and measurements are commonly taken at a fixed φ_{inc}. This invariance illustrates the robustness of the design. Figures 24 and 25 show the frequency response of the metal and slot spiral, respectively, for when θ_{inc} is swept. The center frequency in both graphs is the same, i.e. stable; however, the attenuation in the TE$_{00}$ and TM$_{00}$ mode are no longer symmetric. The two modes have similar values near the center frequency. However, at values above $\theta_{inc} = 30°$ the two modes noticeably diverge off of the center frequency.
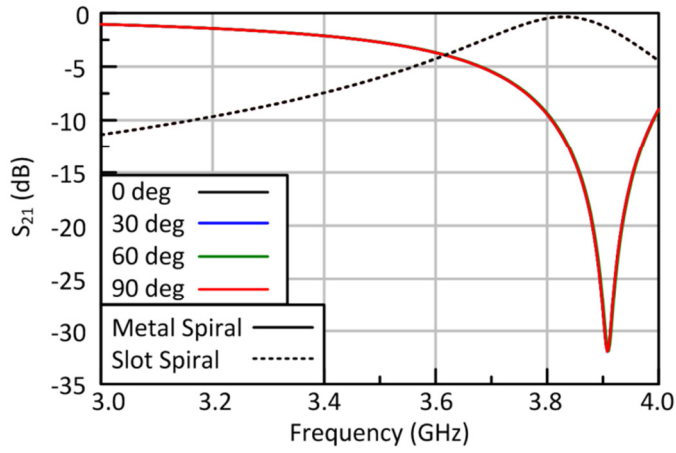
Figure 24 *The frequency response of the four-arm spirals when φ_{inc} is swept. There are multiple lines with different colors, but the curves lie on top of each other.*
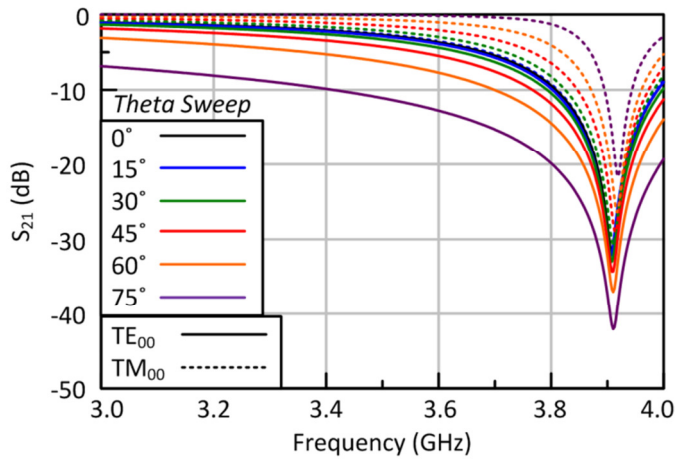
Figure 25 *The frequency response of the Floquet modes of the spiral as θ_{inc} is swept.*
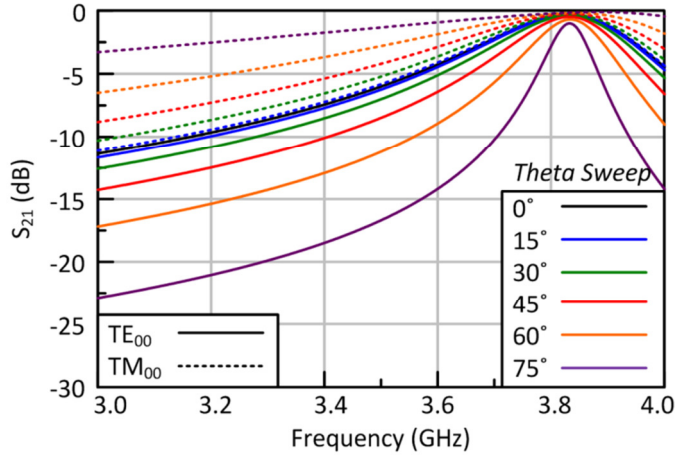
Figure 26 *The frequency response of the four-arm slot spiral with different θ_{inc}.*

3.5.   Other Multi-arm Designs

In addition to the four-arm spiral, other multi-arm spirals can be made using the Archimedean spiral as the base. Figure 27 shows the simulated time average electric fields for one, two, three, and eight arm spirals. Table 1 lists the design parameters for these spirals. Like the four-arm spirals, the two-, three-, and eight-arm spirals show similar quarter wave PCPW transmission line resonator behavior with even and odd numbered arms operating in even and odd quasi-TEM modes, respectively. However, the one-arm spiral operates differently. The middle of this spiral is not a short. The center frequency for this design is 3.94 GHz, and its inner curve length is 26.06 mm. This corresponds to an electrical length of $0.359\lambda_g$, which means it function differently than its multi-arm counterparts. The electrical size of the spirals is smaller than $0.2\lambda_0$, but as more arms are added the electrical size increases in order to accommodate the increase in the number of arms.

Table 1 - Spiral Design Parameters

N_a	N_t	w (mm)	s (mm)	D (mm)	t (μm)	ES*
1	2.73	0.600	0.311	6.40	35	0.070
2	1.90	0.300	0.300	5.75	35	0.067
3	1.225	0.600	0.408	9.95	35	0.112
8	0.71	0.600	0.408	15.92	35	0.165

* This value was calculated using the resonant frequency of the TE_{00} mode for the metal spiral
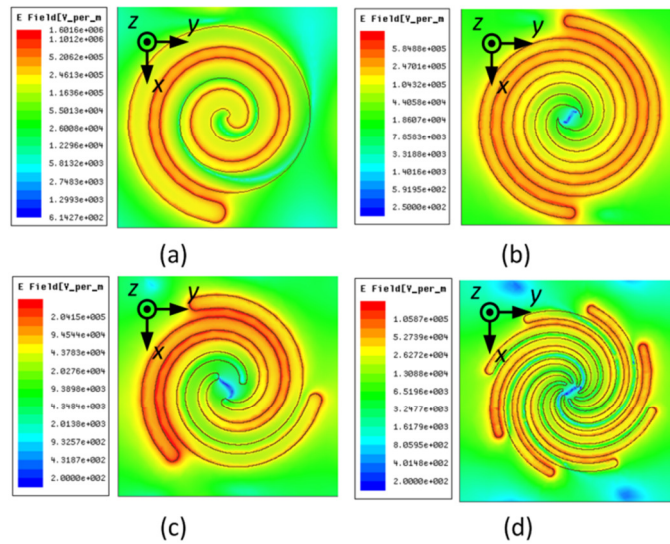
Figure 27 Time average electric field plots of one- (a), two- (b), three- (c), and eight- (d) arm spirals.

Figures 28 through 31 show the simulated frequency responses for the one-, two-, three-, and eight-arm metal spirals. Analysis is limited to the metal spiral because the complementary nature of the metal and slot geometries has been established so the performance of the slot spiral can be extrapolated based on the metal spiral results. The one- and two-arm spirals show suppression for the TE_{00} mode, but have a very weak

response for their TM_{00} mode. This is due to their lower degree of symmetry. The simulated results in figures 27 and 28 illustrate that when the spiral is rotated 90° in the unit cell the TE_{00} and TM_{00} modes switch levels of suppression. These results indicate that the frequency response of the one- and two- arm spirals is polarization dependent, which is similar to the results in [16]. Simulations show that the three-arm spiral has a resonant frequency of 3.92 GHz for the TE_{00} mode and 3.90 GHz for the TM_{00} mode. This difference arises due to the three-arm geometry not being symmetry in the x-y plane, which results in the nearest neighboring coupling being different for each mode. The eight-arm spiral has symmetric frequency response for the TE_{00} and TM_{00} modes. Like the four-arm spiral, the eight-arm spiral has symmetry in the x-y plane.
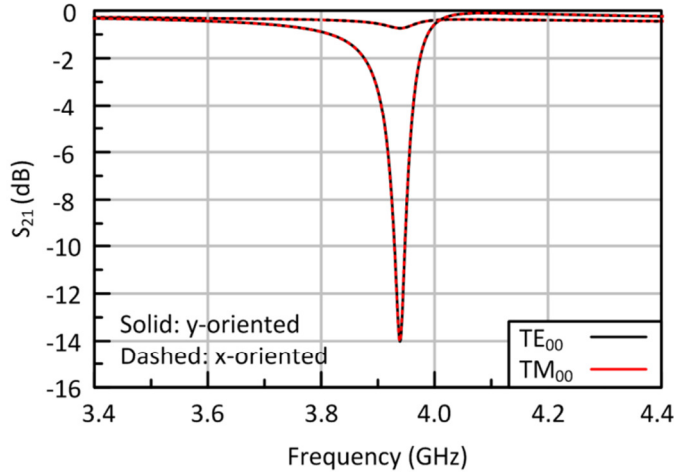
Figure 28 *The frequency response of a one-arm spiral for two different orientations.*
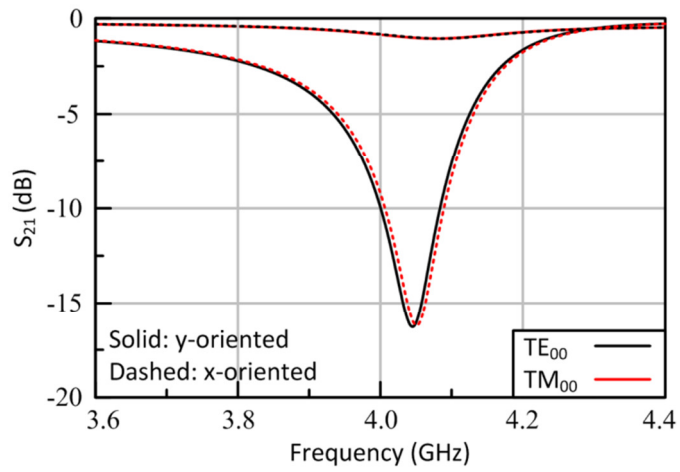
Figure 29 *The frequency response of a two-arm metal spiral for two different orientations.*
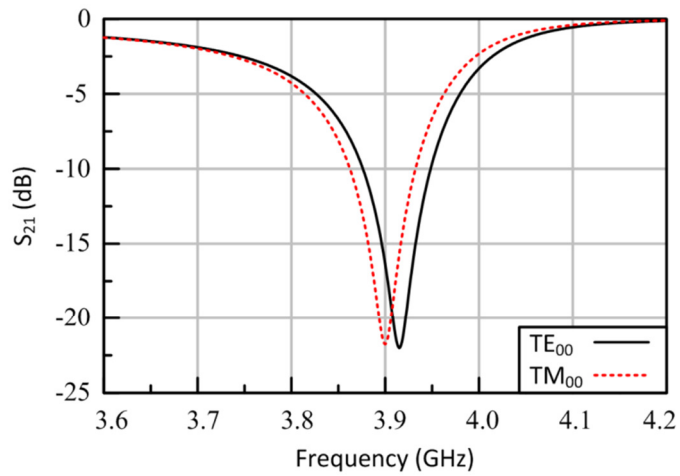
Figure 30 *The frequency response of a three-arm metal spiral has different resonant frequencies for each of its propagating modes.*

43
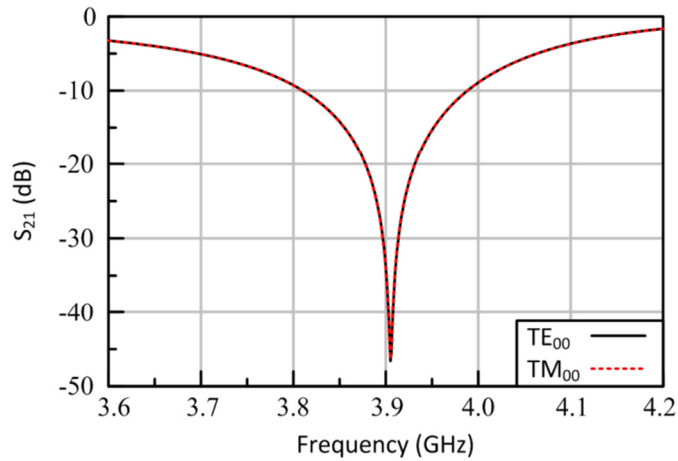
Figure 31 *The frequency response of an eight-arm metal spiral has symmetric TE_{00} and TM_{00} modes.*

Figure 32 shows the normalized frequency response of the one-, two-, three-, four-, and eight-arm spirals. The frequency is normalized to the center frequency of each design. The Floquet mode of interest is the TE_{00} mode. The simulations show that as the number of arms increases the suppression at the center frequency increases. Adding more arms is equivalent to adding more zeros, or poles, to the surface's equivalent transfer function. The bandwidth doesn't behave similarly because its behavior is tied to the nearest neighbor coupling. Multi-arm Archimedean spirals operate in a PCPW transmission line resonator mode, but not all of the designs have modal symmetry, and additional arms increases the electrical size of the resonator.
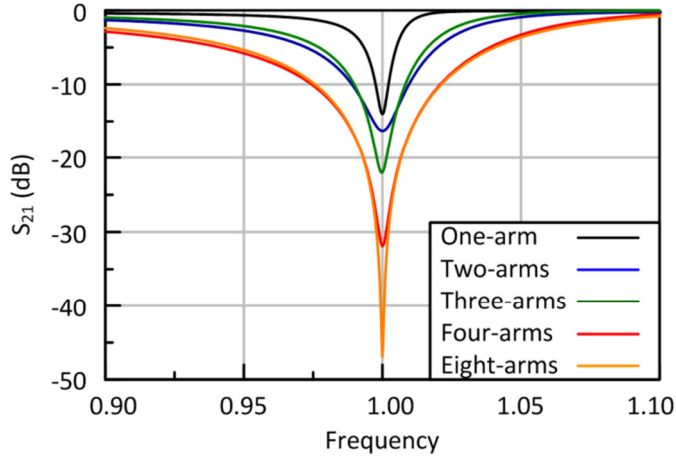
Figure 32 *A plot of the normalized frequency responses for the one-, two- three-, four-, and eight-arm spirals.*

3.6. Higher Order Harmonics

Transmission line resonators are harmonic structures. Quarter wave resonators have resonances every odd multiple of $\lambda_g/4$ with

$$f_n = (2n-1)f_0 \tag{30}$$

where n represents the order of the harmonic, and f_0 represents the fundamental frequency. Spiral FSSs are no different. Figure 33 shows the simulated results for the metal and slot spiral up to 14 GHz. The second resonance occurs at 12.04 GHz for the metal spiral and at 11.64 GHz for the slot spiral. The second harmonic occurs when the electrical length is equal to $3\lambda_g/4$. In between the resonances there is a maximum for the metal spiral at 4.51 GHz and a minimum at 4.67 GHz for the slot spiral. These are referred to as anti-resonant points. Between two resonant points there has to be an anti-resonant point [54]. Physically, these anti-resonant points represent the discontinuities on the reactance curves of the surface where the reactive value jumps from positive

45

infinity to negative infinity. This transition has to happen between two resonant points. The presence of these harmonics is beneficial in that the surface can have multiple operational bands while only having one resonator.
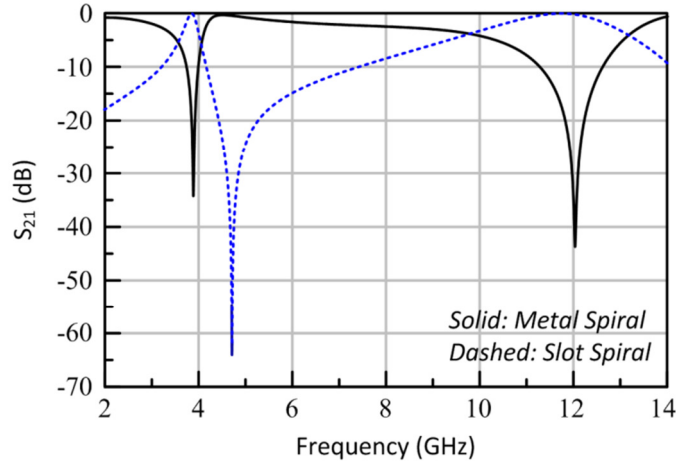
Figure 33 Simulations show that higher order resonances occur in the four-arm spiral.

3.7.   *Dielectric Effects*

FSSs are typically fabricated on low loss dielectric substrates. For single layered surfaces the substrate is for mechanical support, but for a multi-layered structure the substrate is integrated into the design as an impedance transformer [2]. Several papers have analyzed the effects that dielectrics have on the resonant frequency [55-57]. Most authors when designing a FSS use

$$\varepsilon_{reff} = \left(\frac{\varepsilon_r + 1}{2} \right) \tag{31}$$

as a first order approximation for a single layer substrate with the copper trace on the air dielectric boundary. For the Archimedean spiral this is not necessarily true.

46

It was shown that the four-arm metal spiral operates in a periodic coplanar transmission line configuration with an even mode field distribution. The authors in [50] give a closed form expression using conformal mapping for the effective dielectric constant of a periodic coplanar transmission line for both even and odd mode distributions, which includes stratified media. Figure 34 shows the calculated effective dielectric constant using the four-arm design parameters and substrate properties. For thin substrates the effective dielectric constant is closer that of air, but for thicker substrates the ε_{reff} approaches an asymptotic value, which is the same as the one calculated from (31). For stratified substrates the conformal mapping equations are only valid for monotonically increasing or decreasing dielectric constants. The conformal mapping formulas cannot be used for random dielectric layers.
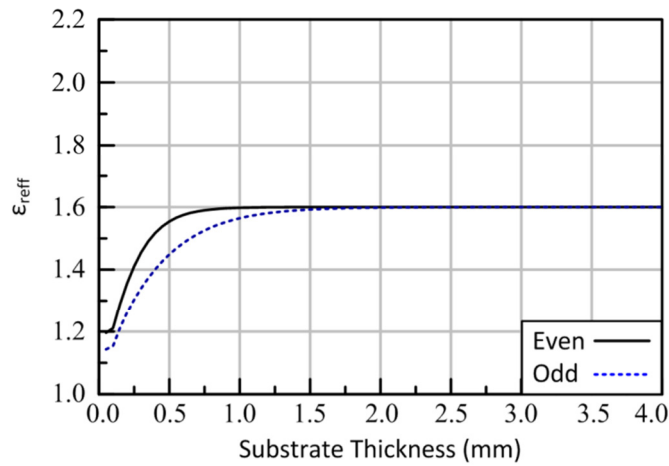
Figure 34 *The calculated effective dielectric constant using the four-arm spiral design parameters and substrate properties.*

Another contribution the dielectric loading is the shape of the resonator. To investigate this two FE models were simulated: one model was the traditional slot dipole, and the other model was a four-arm slot spiral. Figure 35 shows the expanded 3-D model of the slot spiral. Both models had 1.575 mm thick substrates made of Duroid 5880, and PDMS superstrates of a variable height.

Figure 36 shows the center frequency versus superstrate thickness for a dipole slot and a slot spiral design. The center frequency for the slot spiral approaches the asymptotic value of 3.05 GHz rather quickly. By the time the superstrate has a thickness of $0.01\lambda_0$ the FSS has reached its asymptotic value. This means that for a stratified medium the first several layers will have a larger impact on the center frequency than the final layers. A drawback to this is that thin bonding layers close to the surface are not negligible.

In contrast, the slot dipole's resonant frequency decreases at a slower rate than the slot spiral and begins to slowly oscillate around the frequency of 3.05 GHz. Similar oscillatory behave was observed in [55] for other geometries. The authors contribute this oscillatory behavior to low order evanescent modes that decay slowly away from the surface. Another study was conducted by the same authors on the shape dependence for dielectric loading [57]. They compared three resonator shapes: the dipole, the circular patch, and the square loop. Their results showed that the Floquet modes of the resonator's geometry affect the amount of stored energy near the surface. With the dielectric being right at the surface this implicitly affects how much energy is stored in the dielectric. With more energy stored near the surface the dielectric layer will have a

48

larger influence on the resonant frequency. Their simulations showed that the square

loop's fields decayed the fastest, and the circular patches decayed the slowest. A similar

comparison is seen between the slot spiral and slot dipole.
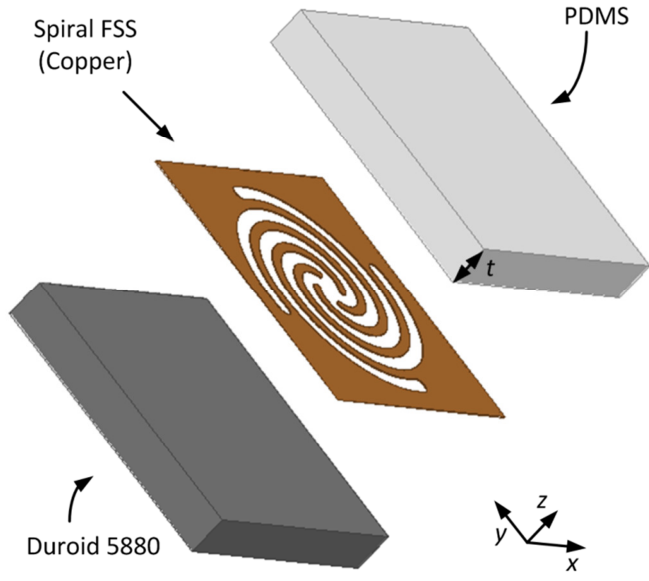
Figure 35 *An expanded view of the slot spiral's unit cell with a PDMS superstrate of variable thickness.*
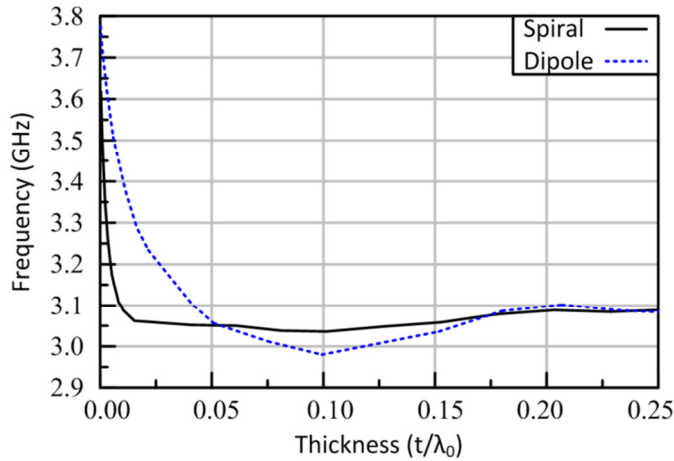
Figure 36 A plot of the slot spiral and slot dipole's center frequency function of superstrate thickness.

3.8.   *Effects of the Lattice Structure*

Section 3.4 showed that a four-arm spiral has symmetric TE_{00} and TM_{00} Floquet

modes. This modal symmetry is caused by the geometric symmetry. However, there are

two geometric attributes here: the spiral geometry and the lattice structure. The previous

four-arm spiral is in a square lattice, which has the same axis of symmetry as the spiral.

It is unclear whether this modal symmetry will remain when the lattice geometry is

different.

Figures 37 through 40 show the frequency response of a four-arm Archimedean

spiral in a triangular lattice with a slant angle $\Omega = 60°$. The only design parameters that

changed from the previous four-arm design were the unit cell size with $D_x = 11.50$ mm

and $D_y = 0.866D_x$. The thickness of the copper is 35 μm for both the metal and slot

spirals. These changes resulted in the resonant frequency increasing due to a decrease in

the nearest neighbor coupling. Simulations showed that the resonant frequencies of the

50

two modes differed by at most 20 MHz. This is a minor breaking in symmetry, and outside of ultra-narrow band applications this breaking is negligible. A lattice structure with a different level of symmetry, e.g. six-fold symmetry, might create a larger breaking in symmetry.
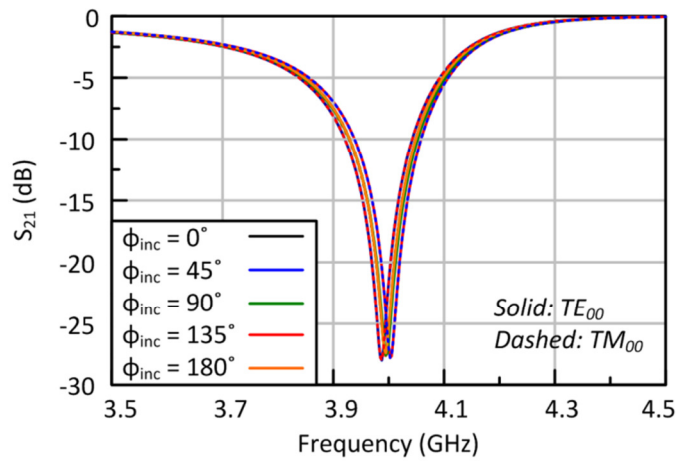
Figure 37 *The frequency response of a four-arm metal spiral in a triangular lattice at different φ_{inc}.*
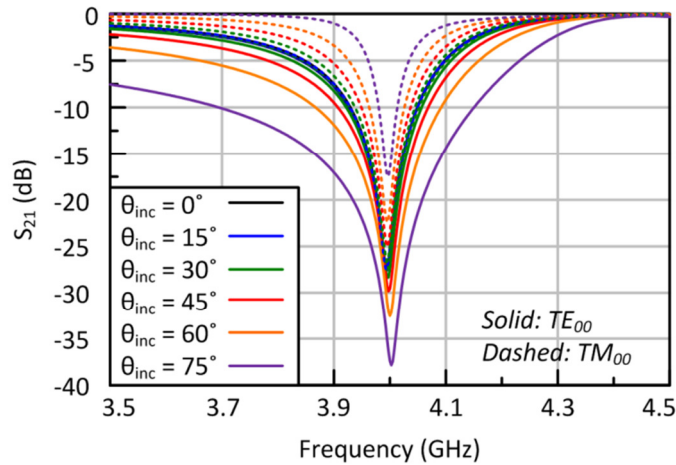
Figure 38 *The frequency response of a four-arm metal spiral in a triangular lattice at different θ_{inc}.*
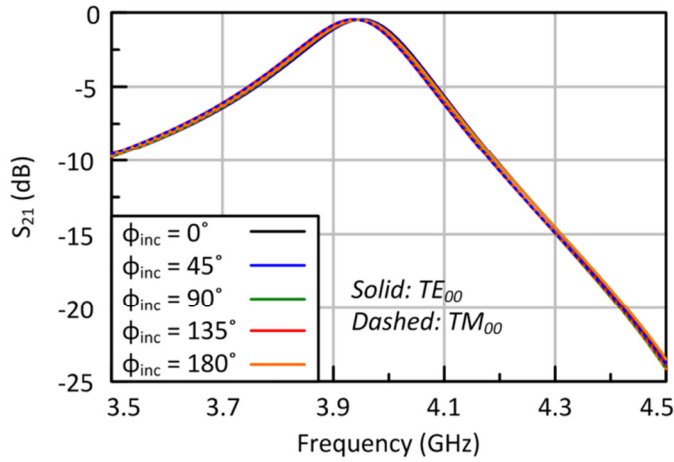
Figure 39 The frequency response of a four-arm slot spiral in a triangular lattice at different φ_{inc}.
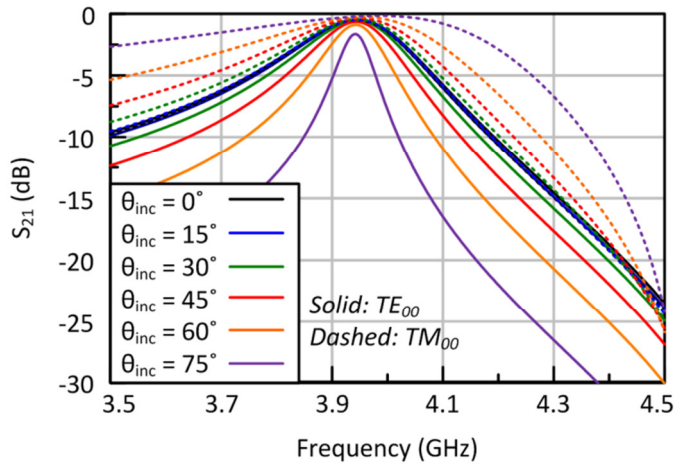
Figure 40 The frequency response of a four-arm slot spiral in a traignular lattice at different θ_{inc}.

Figures 41 through 44 show the frequency response of a four-arm spiral in a hexagonal lattice whose side length $D = 5.5$ mm. This side length was chosen to ensure tight packing of the spirals. All other design parameters remain the same. By changing the lattice structure the nearest neighbor coupling changes. Tighter spiral packing will increase the impact that the nearest neighbor coupling will have on the resonant

52

frequency, and make any breaking in symmetry more pronounced. Simulations show that the largest frequency difference between the modes is 75 MHz for when $\varphi_{inc} = 60°$. Similar behavior is observed in the slot spiral with the maximum difference between modal resonant frequencies being 57.5 MHz when $\varphi_{inc} = 60°$. This mismatch in axis of symmetry broke the frequency stability of the structure.
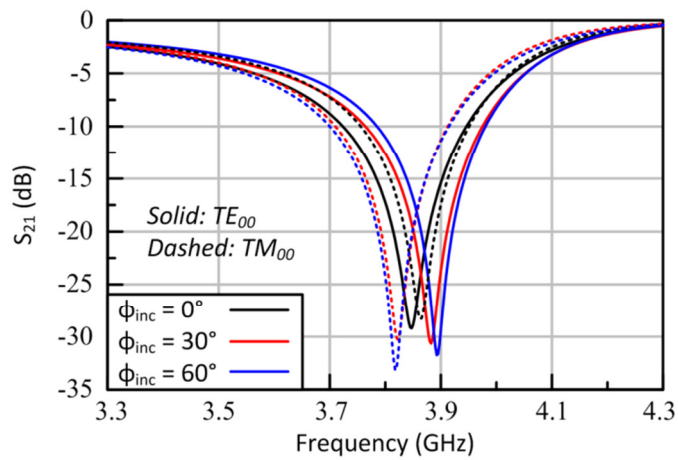
Figure 41 *The frequency response of a four-arm metal spiral in a hexagonal lattice at various* φ_{inc}.
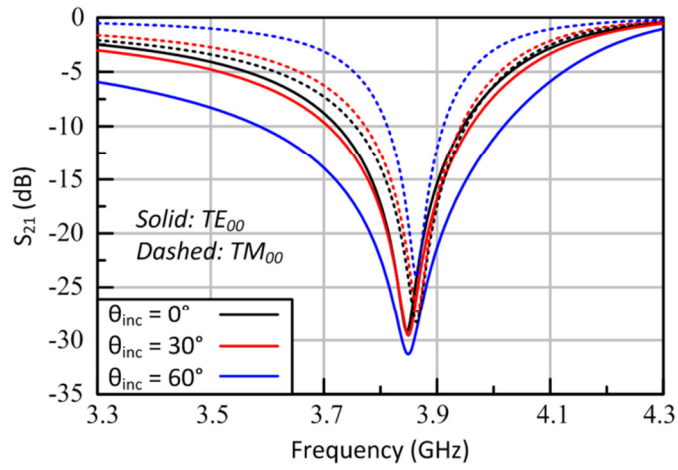
Figure 42 *The frequency response of a four-arm metal spiral in a hexagonal lattice at various θ_{inc}.*
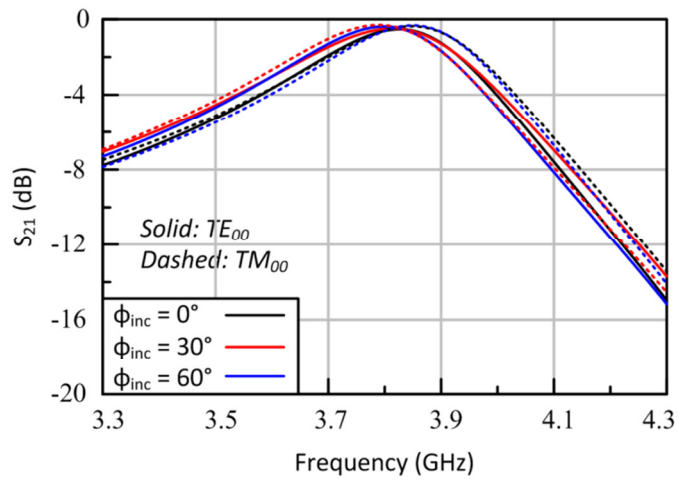
Figure 43 *The frequency response of a four-arm slot spiral in a hexagonal lattice at various φ_{inc}.*
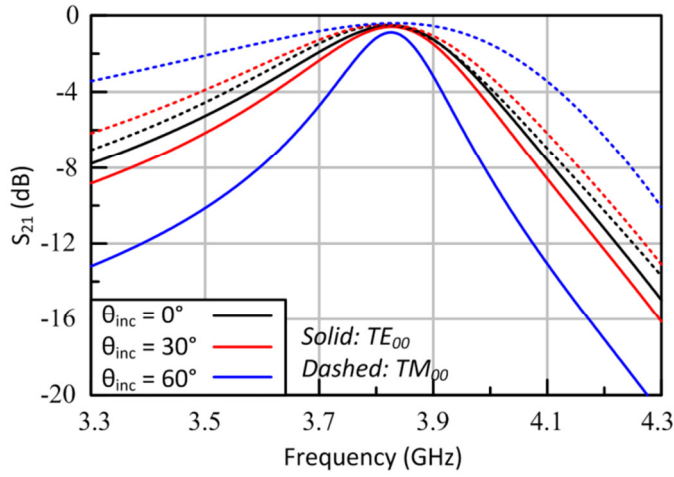
Figure 44 *The frequency response of a four-arm slot spiral in a hexagonal lattice at various θ_{inc}.*

Figures 45 through 48 display the frequency responses of a six-arm spiral in a hexagonal lattice at various incident angles. The design parameters for the six-arm spiral are $w = 0.3$ mm, $s = 0.3$ mm, $N_t = 1.125$, $t = 35$ µm, and $D = 5.5$ mm. The behavior in these figures is similar to the behavior seen with the four-arm spirals in a square lattice. The results for φ_{inc} had the same frequency response illustrating that a six-arm spiral in a hexagonal lattice is invariant under a φ_{inc} rotation. Both metal and slot spirals show modal symmetry and frequency stability for multiple incident angles. The takeaway from the above results is that for a tightly packed spiral the lattice structure has to have same axis of symmetry as the resonator in order to have modal and frequency stability.
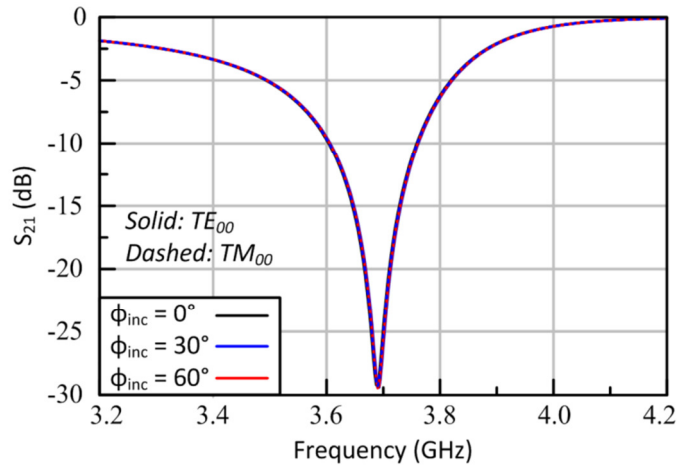
Figure 45 *The frequency response of a six-arm metal spiral in a hexagonal lattice versus φ_{inc}.*
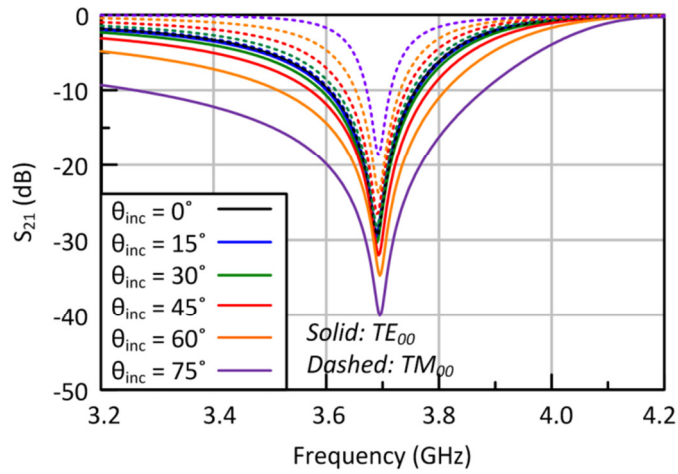
Figure 46 *The frequency response of a six-arm metal spiral in a hexagonal lattice at various θ_{inc}.*

56
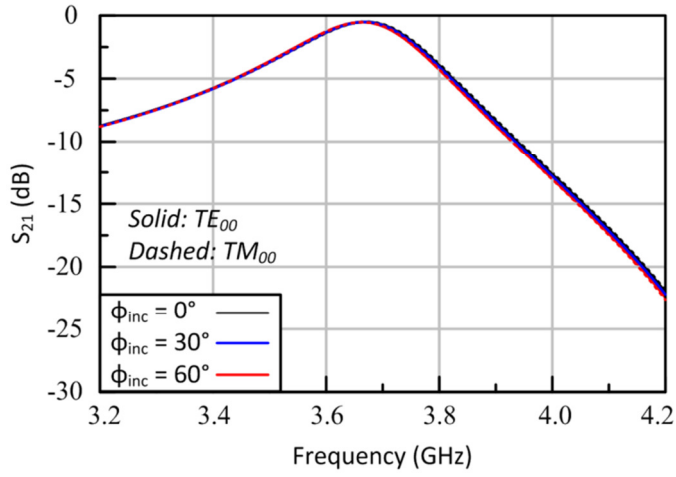
Figure 47 The frequency response of a six-arm slot spiral in a hexagonal lattice at various φ_{inc}.
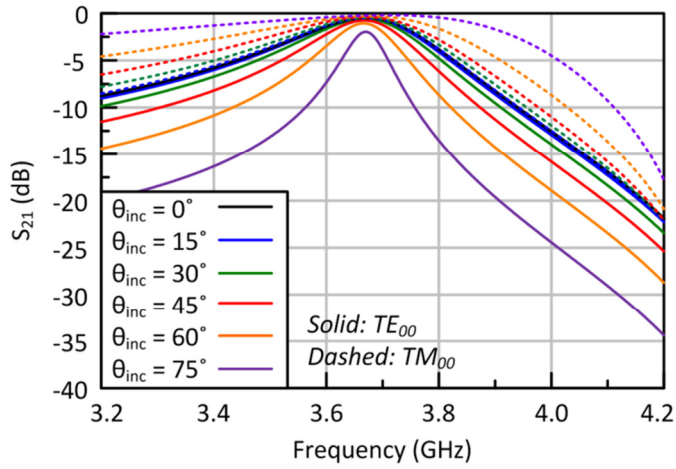
Figure 48 The frequency response of a six-arm slot spiral in a hexagonal lattice at various θ_{inc}.

3.9. Equivalent Circuit Model

Quarter wave transmission line resonators have lumped element equivalents. The texts [58, 59] go through the derivation for the general RLC values. The following analysis is limited to the four-arm spiral case in order to simplify the analysis to the TE_{00} case because of modal symmetry. Based on the electric field plot in Figure 14 the metal

57

spiral's arms are treated as a transmission line terminated in an open circuit; based on the surface current plot in Figure 16 the slot spiral's arms end in a short circuit. As stated in section 3.5 each additional arm behaves like a degenerate pole and zero in the surface's equivalent transfer function. Using [54] as a template for general LC resonators, Figure 49 illustrates the equivalent circuit model for the metal spiral; Figure 50 illustrates the equivalent circuit model for the slot spiral. The substrate and superstrate are represented by a dielectric filled transmission line with

$$Z_0 = \frac{377\Omega}{\sqrt{\varepsilon_{reff}}}. \tag{32}$$

For a FSS the excitation is a plane wave which is represented by infinite transmission lines with a $\eta_0 = 377$ Ω. The inductance and capacitance of the spirals are related by

$$f_0 = \frac{1}{2\pi\sqrt{LC}}. \tag{33}$$

The equivalent inductance and capacitance of the spiral are

$$C = \frac{4}{N_A \pi Z_0 \omega_0}; \quad \text{metal spiral} \tag{34}$$

$$L = \frac{4Z_0}{N_A \pi \omega_0}; \quad \text{slot spiral.} \tag{35}$$

The equivalent resistance represents conductor loss

$$R = \alpha N_A Z_0 d \quad \text{metal spiral}$$
$$R = \frac{N_A Z_0}{\alpha d} \quad \text{slot spiral,} \tag{36}$$

where d is the effective length of the arms, and the attenuation constant α is approximated by the formulas listed in [60] for coplanar waveguides and strips.

Conformal mapping techniques have been applied to periodic transmission line structures to solve for their characteristic impedance, Z_0, and effective dielectric constant, ε_{reff} [50]. This is a quasi-static approach requiring

$$\frac{\lambda_g}{2} \gg w_g + w + 2s, \tag{37}$$

where w_g is the width of the ground line. For the four-arm design $w_g = w$, $\lambda_g = 38.36$ mm, and $w_g+w+2s = 2.016$ mm. The design parameters meet the conformal mapping requirement. Further research can be done by using the conformal mapping techniques in [50] for a more accurate calculation of the conductor losses, but that is beyond the scope of this work. Also, any energy coupling into surface waves is also assumed to be zero.

To accurately model the resonance of interest the other harmonics need to be included. However, it is sufficient enough to include the surrounding harmonics outside the band of interest. For example, if a designer wanted to model the frequency band containing f_2 then the circuit model should include f_1 and f_3 even though they are outside the band of interest.

The length extensions are lumped into a single term added to the physical length, and is used to calculate f_0. The nearest neighbor coupling is the dominant second order effect, and is represented by an extra reactive component. For the metal spiral this element is represented by a series capacitor, and for the slot spiral it is a parallel inductor. The coupling and length extensions are extracted by curve fitting the circuit model results to full wave simulations. Circuit models of the three-, four-, and eight-arm spirals were simulated using Keysight's™ Advanced Design System™ (ADS). A built

59

in quasi-Newton optimization algorithm was used to extract the nearest neighbor

coupling and length extension terms. Table 2 lists the equivalent length extension and

coupling values extracted from the optimization process. It should be noted that for the

three-arm spiral the effects of the higher order mode needed to be curve fitted because

the pole/zero between the harmonics was close to the first harmonic's operating band,

and the theoretical RLC values corresponding to f_2 did not accurately model this. The

next harmonic was thus represented by its dominant reactive component, e.g. a capacitor

for the metal spiral, and set as an optimization variable. The corresponding component

values are 33.42 fF for the metal spiral and 895.5 pH for the slot spiral. In addition, if the

TE and TM modes are not symmetric the curve fitted values will be different depending

on the mode of interest. The simulated values presented are from the TE_{00} mode because

that is the only mode that can be measured with the lab equipment. Circuit model results

are presented and discussed along with FE and measured results in section 4.
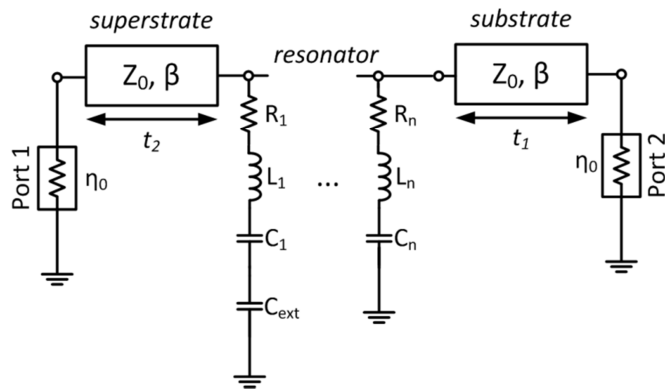
Figure 49 *The equivalent circuit model for the metal spiral.*

60
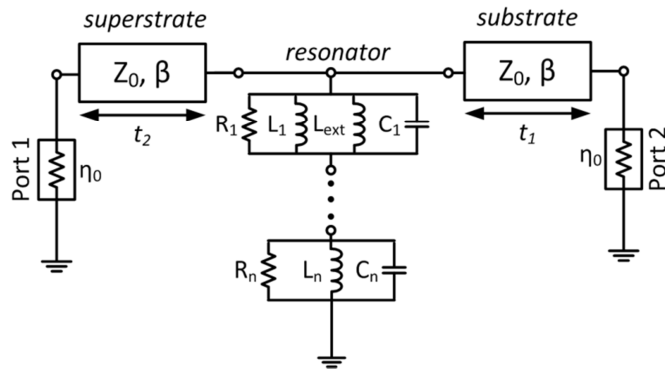
Figure 50 *The equivalent circuit model for the slot spiral.*

Table 2 - Optimized Circuit Model Parameters

FSS Type	Length Extension (mm)	Coupling Term
3-arm BS	0.124	11.84 fF
3-arm BP	0.345	269.6 pH
4-arm BS	0.759	42.25 fF
4-arm BP	0.998	833.7 pH
8-arm BS	0.697	69.92 fF
8-arm BP	0.677	1.897 nH

4. EXPERIMENTAL SETUP AND MEASURED RESULTS

4.1.   *Waveguide Test Fixture*

Common measurement methods for FSSs involve a free space experimental

setup inside an anechoic chamber. The authors in [21] give a general description for

several free space setups. As stated previously, the band of interest for this work is 2-4

GHz. At 2 GHz the free space wavelength is 150 mm. In order to reduce measurement

error from edge diffractions the test surface needs to be quite large. An alternative

measurement setup is to use a waveguide system [61]. Some authors have used this

method to experimentally verify the operation of their FSS [27, 32, 62]. However, unlike

free space setups a waveguide is dispersive. The fields in a waveguide are frequency

dependent. Figure 51 shows the calculated equivalent incident angle for the proceeding

waveguide setup across its operating frequency based on the reflected plane wave model.

Calculations show that the incident angle becomes more oblique at lower frequencies.
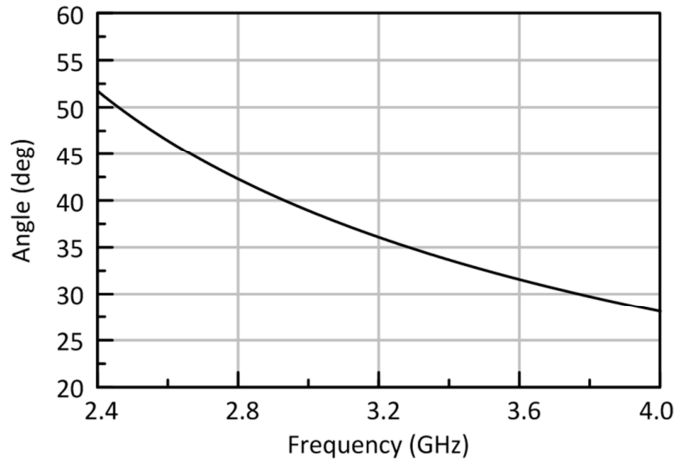
Figure 51 *A plot of the equivalent incident angle based on the plane wave decomposition of a waveguide mode.*

Figure 52 shows the experimental setup used to measure the frequency response of the fabricated surfaces. A WR-284 waveguide launcher excites the system. Its manufacturer recommended operating frequency is 2.6 to 3.95 GHz, but its range is extended to 2.4 to 4 GHz. The cutoff frequency for the TE_{10} mode is 2.08 GHz and 4.16 GHz for the TE_{20} mode. Attached to the launcher are two waveguide segments. These sections have a square cross sectional area with a side length of 79.6 mm. The length of each segment is ℓ_l = 162.9 mm. The launcher's aperture has a cross sectional area of 72.136 mm by 34.036 mm. The cross sectional mismatch between the two pieces adds a reactive component to the system at the junction. Figure 53 shows the equivalent circuit model of the unloaded system before calibration.
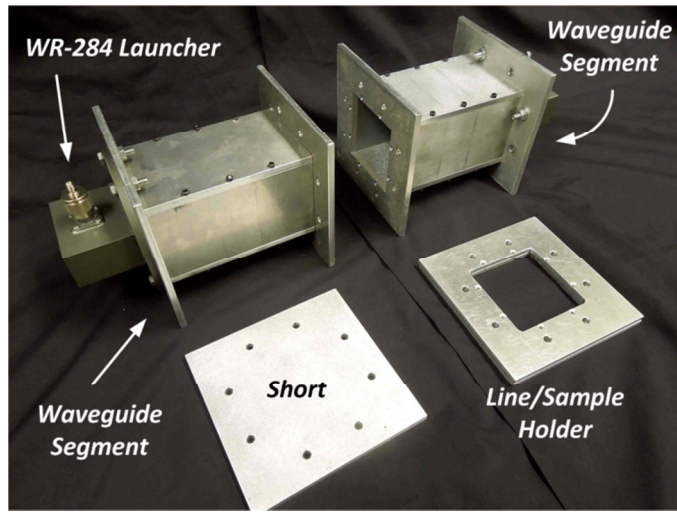
Figure 52 *The waveguide experimental setup and the TRL calibration kit.*
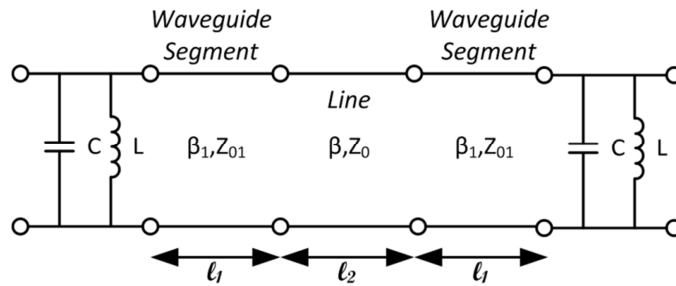
Figure 53 *The equivalent circuit of the experimental setup before calibration.*

To remove the reactive step the system is calibrated with a TRL standard. The line standard has a length of $\ell_2 = 13.2$ mm. The reference plane is set to the ends of the waveguide segments. Time domain gating is applied to the measurements to suppress unwanted secondary reflections. The FSS fits inside the line standard.

4.2. Multi-arm Spiral Measured Results

Both metal and slot spiral surfaces were fabricated on 1.575 mm Duroid 5880

substrates using a combination of mechanical milling and chemical etching techniques.

The three- and four-arm spiral surfaces lie in an 8 by 8 square grid, and the eight-arm

spirals lie in a 5 by 5 grid. These lattices were chosen so the surfaces would fit inside the

waveguide measurement system. Figure 54 shows the fabricated three-, four-, and eight-

arm surfaces.
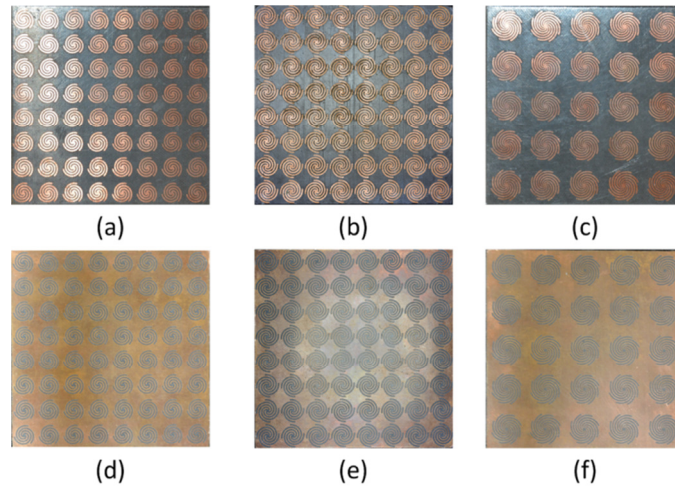
Figure 54 The fabricated surfaces of the three-arm metal (a) and slot (c) spirals, four-arm metal (b) and slot (e) spirals, and eight-arm metal (c) and slot spirals (f).

Table 3 lists the center frequencies and insertion losses of the measured surfaces

compared to the FE and circuit models. Figures 55 through 60 show the simulated and

measured results for the three-, four-, and eight-arm surfaces. All of the surfaces display

the designed band-stop and band-pass behavior, and are within 1-2% of their simulated

values. The circuit model is in very good agreement with the FE model. The largest

65

difference was the measured eight-arm spiral's center frequency being 1.5% higher than simulation. The difference in the resonant frequencies is caused by the fabrication process.

Table 3 - Measured FSS Results

FSS Type	f_0 (GHz)*	IL (dB)*	f_0 (GHz)**	IL (dB)**	f0 (GHz)***	IL (dB)***
3-arm BP	3.807	2.193	3.849	0.816	3.850	0.028
3-arm BS	3.925	18.74	3.920	34.33	3.911	46.87
4-arm BP	3.776	0.742	3.830	0.347	3.835	0.037
4-arm BS	3.890	22.44	3.910	31.86	3.906	49.83
8-arm BP	3.800	0.280	3.837	0.229	3.839	0.072
8-arm BS	3.961	46.89	3.905	34.54	3.902	44.10

* measured, ** FE model, *** CM
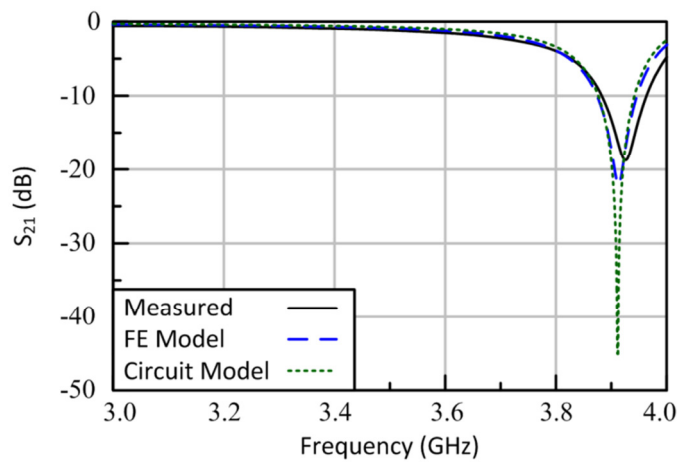
Figure 55 *Simulated and measured results for the three-arm metal spiral.*
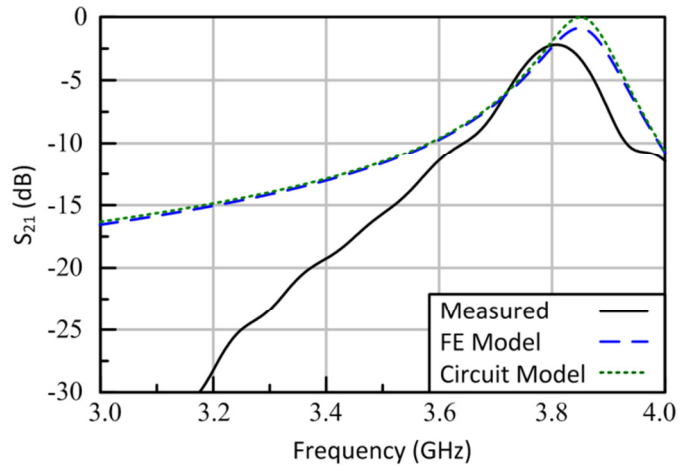
Figure 56 Simulated and measured results for the three-arm slot spiral.
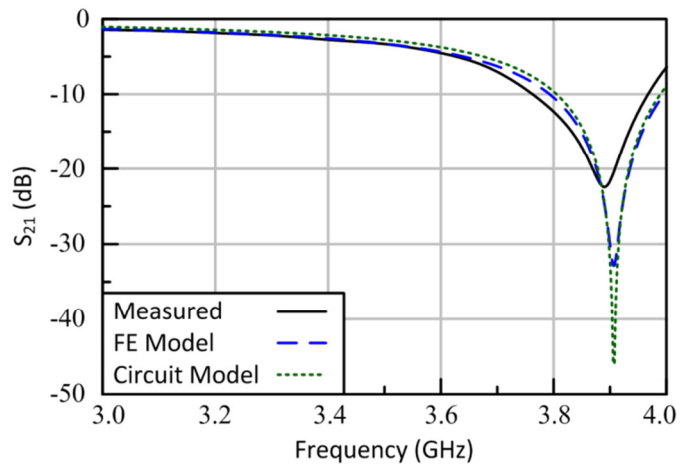
Figure 57 Simulated and measured results for the four-arm metal spiral.
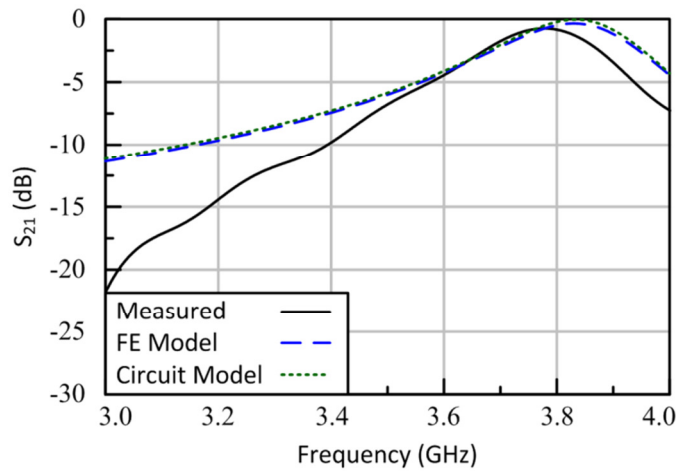
Figure 58 Simulated and measured results for the four-arm slot spiral.
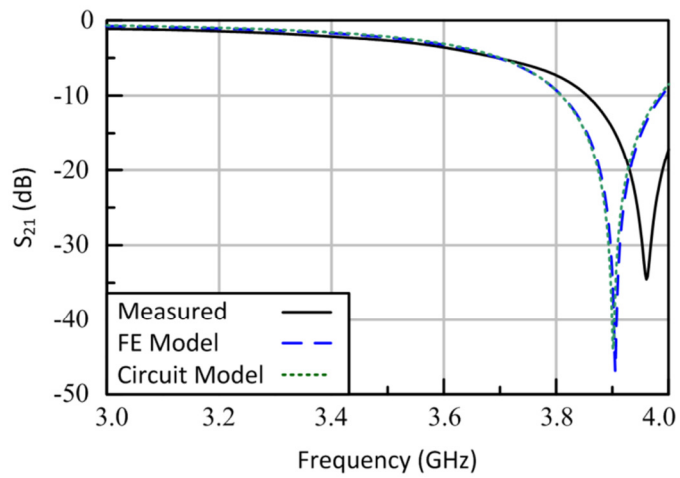
Figure 59 Simulated and measured results for the eight-arm metal spiral.

68
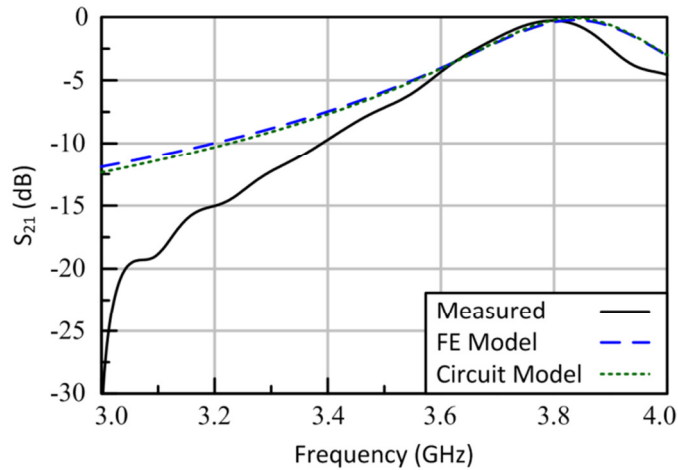
Figure 60 *Simulated and measured results for the eight-arm slot spiral.*

Aside from the four-arm metal spiral, all of the other surfaces were fabricated using chemical etching. The etching process is isotropic. For isotropic processes there is a larger amount of copper removed due to lateral etching versus an anisotropic process [63]. The center of the metal spirals and ends of the slot spirals are most the susceptible to this. This increase in lateral etching makes the arms physically and electrically longer, which decreases the resonant frequency. This adds a source of error. In addition, the substrates that were used had copper annealed to both sides. To remove this copper the boards were left in the chemical bath longer than was necessary to remove the spiral traces. This prolonged time in the chemical bath increases the amount of copper laterally etched making the arms longer and shifting the resonant frequency down. All of the surfaces, excluding the eight-arm metal spiral, have lower center frequencies than simulations predict.

For the eight-arm metal spiral it has a different source of error. Unlike the other surfaces, its resonant frequency was higher than predicted. This is due to the age of the chemicals. Discussions with the technicians about the chemical etching process revealed that the freshness of the chemicals affects the precision. For new chemicals the smallest trace that can be made is 0.1 mm wide, and with older chemicals the precision decreases to 0.3 mm. The eight-arm metal spiral's arms taper a little toward the center with the smallest size being 0.181 mm. Older chemicals would not be able to completely etch this out. The arms would thus be shorter. There is no data on the freshness of the chemicals during fabrication. However, with the eight-arm spiral's resonant frequency being higher than the predicted this lends credence to the idea that the chemicals were not new. This under etching at the center of the spiral is a larger source of error than the over etching caused by lateral etching. However, despite these small shifts, the resonant frequencies of the spirals fell within the 3 dB operational bandwidth for all designs.

There was disagreement in the measured insertion loss for all of the surfaces when compared to simulation. The FE models use Floquet theory to simplify the surface to just the unit cell. The frequency response from these simulations corresponds to an infinite surface – not a finite surface. Other loss mechanisms, e.g. surface waves, are present in finite FSSs, which are not present in infinite FSSs. To accurately compare losses, either a free space measurement method should be used or a finite model should be created in simulation.

For all of the slot spiral surfaces the measured results diverge at lower frequencies. There are two phenomena that cause this divergence. The first phenomenon

is the behavior of the surface. The TE_{00} mode's transmitted power decreases as the incident angle increases. Figure 51 showed that the equivalent incident angle of the waveguide mode increases as the frequency decreases. This means that the measurements in the waveguide are frequency dependent. For the metal spiral this doesn't cause a noticeable divergence between measurements and simulations because the metal spiral designs are nearly transparent outside of resonance. In contrast, the slot spiral becomes more opaque at higher incident angles. Since the waveguide is dispersive these effects are present in the measurements, but are not captured in the FE simulations. The FE model is equivalent to a free space model and not a waveguide mode.

The other reason for the slot spiral measurement discrepancy is that off of the center frequency the slot spiral surface becomes reflective. This creates a cavity in the waveguide that the calibration does not account for. The reference plane is set by the reflect standard, which is set at the end of the waveguide segment. The line standard elongates the waveguide section creating a longer cavity backed by the FSS. The drop in transmitted power is due to power coupling into resonant modes. This coupling occurs at the lower end of the frequency span. With the pass-band being near the top of the S-band the excited cavity modes are in the stop-band of the slot spiral FSS, and can be ignored. The measured and simulated results are in good agreement despite some differences caused by fabrication tolerances and measurement effects. The results show that the surfaces have a single resonance near the predicted value, and that the measurement method produces results that are a good general indicator of how the surfaces will behave in a free space environment.

71

4.3.   *Experimentally Observed Polarization Invariance*

Figure 24 shows that the TE_{00} and TM_{00} modes are symmetric versus φ_{inc} at broadside. This modal symmetry implies that a four-arm slot spiral FSS is transparent to circular polarization (CP) in the pass-band. When θ_{inc} is swept the center frequency of the spiral remains the same, but the bandwidth of the modes shrinks. To experimentally test the CP invariance, a larger slot spiral surface was fabricated using chemical etching techniques. The new design had $D = 11$ mm and $N_t = 1.043$ while the rest of the parameters remained the same. The spirals were in a 25 by 23 square lattice. The simulated pass-band is centered at 3.83 GHz with an insertion loss of 0.479 dB and a 3 dB bandwidth of 201.1 MHz.

To test the CP transparency properties of the surfaces left- and right-handed patch antennas are used. Their layout is the same as in [64], but with the feed point being off diagonal to ensure a 90° phase difference between the two near degenerate modes. The antenna's design parameters are the patch width $p_x = 24.4$ mm, patch height $p_y = 25.4$ mm, extra ground plane size $d = 10$ mm, horizontal feed location $f_x = 19.10$ mm (25.45 mm for the LH patch), vertical feed location $f_y = 18.10$ mm (17.9 mm for the LH patch), and trench size $t_s = 1.588$ mm. The patches were mechanically milled on Duroid 5880 with a thickness of 1.575 mm.

The antennas and FSS are measured in an anechoic chamber using a linearly polarized pyramidal horn antenna as the reference antenna. The antenna is rotated 90° to test the horizontal polarization. Figure 61 depicts the experimental setup used in the chamber. The distance the FSS rests away from the antenna was found experimentally to

be a = 11.4 cm. The metrics for assessing this were to observe when the FSS minimally affects the load impedance and VSWR of the antenna. To test the effects of the spiral's chirality the surface is flipped from the copper side facing outward, RH spiral, to inward, LH spiral.
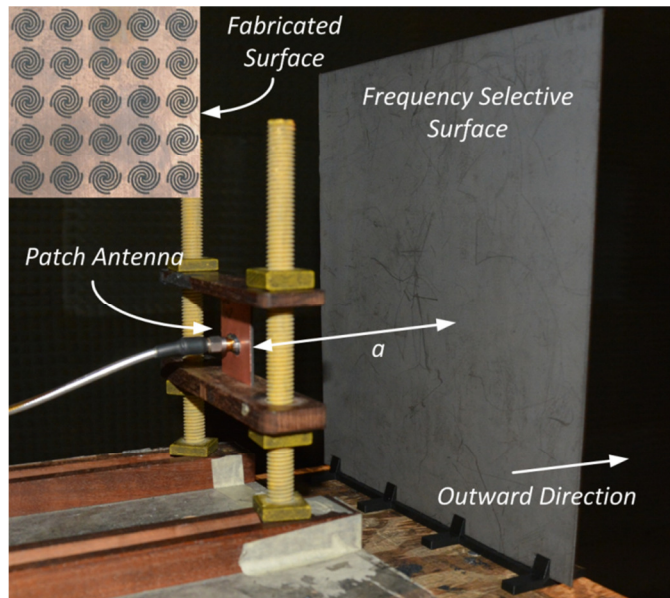
Figure 61 *The experimental setup for the antenna and FSS. The inset is the fabricated surface.*

Table 4 lists the benchmarks for the antennas in the various configurations. The operating frequencies listed are taken at the operating frequency of the antenna without the FSS in order to offer a quantitative comparison. Figure 62 shows the load impedance of the LH (a) and RH (a) antennas. The antenna's operating frequency is defined as the point where the modes are degenerate in the absence of the FSS. The antenna's target center frequency was 3.80 GHz. This value was chosen in anticipation of frequency shifts caused by over-milling and etching. The measured operating frequency of both

antennas was found to be 25 MHz higher than simulations predicted. This shift is due to over-milling around the perimeter of the copper patch. A second round of simulations was performed with a trench that spanned the perimeter of the copper patch whose width is the same as the mill bit's head t_s. This trench represents over-milling. With the trench included the simulated values are in closer agreement with the measured results. The corresponding trench depths are 0.152 mm and 0.114 mm for the LH and RH CP antennas, respectively. Figure 63 shows the VSWR of the LH (a) and RH (b) antennas in the presence of the FSS. The surface minimally affects the antennas' impedance matching by slightly shrinking the VSWR bandwidth. This decrease is to be expected because the surface becomes more electromagnetically opaque outside of its operating band. The greatest decrease in bandwidth was 30 MHz for the LH spirals in front of the LH antenna. This minimal perturbation of the antenna's matching and load impedance shows that around the operating frequency the surface appears transparent to the antenna.

Table 4 - Antenna Benchmarks

	f$_0$ (GHz)	VSWR	VSWR BW (GHz)	AR (dB)	PD (deg)
LH Ant. – Sim. #2	3.823	1.052	0.182	0.116	93.85
RH Ant. – Sim. #2	3.827	1.048	0.182	0.248	-92.48
LH Ant. – Meas.	3.825	1.067	0.185	0.839	78.05
RH Ant. – Meas.	3.823	1.082	0.188	1.062	-94.58
LH Ant. w/ FSS	3.816/3.816	1.067/1.083	0.168/0.155	1.479/1.591	97.50/97.30
RH Ant. w/ FSS	3.828/3.826	1.092/1.077	0.180/0.180	1.338/1.742	-83.63/-83.60

The rows with two values listed represent measurements for the LH and RH spiral surfaces, respectively.
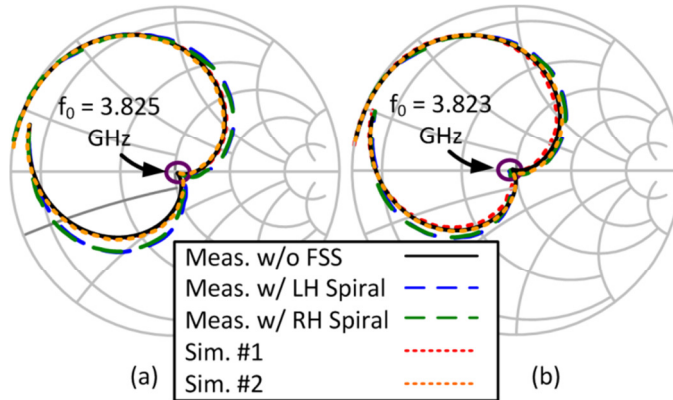
Figure 62 *The load impedance of the LH (a) and RH (b) antennas in the presence of the FSS.*
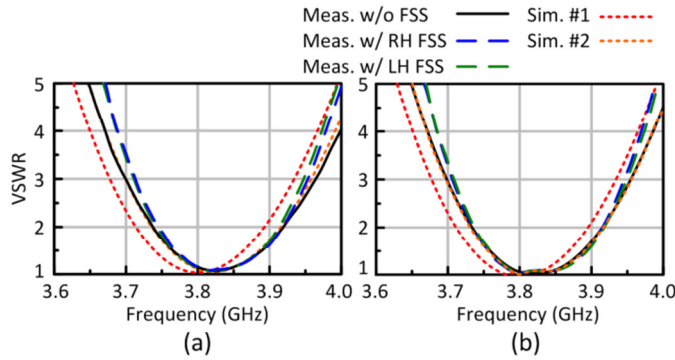
Figure 63 *The measured VSWR of the LH (a) and RH (b) antennas in the presence of the FSS.*

Figures 64 and 65 show the measured axial ratio and phase difference of the

antennas in the presence of the FSS. There is an increase in the axial ratio of the

antennas in the presence of the FSS, but this is still within the 3 dB CP operational

bandwidth. The phase measurements slightly disagree for all of the experiments. There

was unavoidable cable movement when taking the cross polarization measurements;

however, the handedness of the wave is still apparent in all of the measurements. There

is a negligible difference in operation of the antenna when the chirality of the surface is

changed. Figures 66 and 67 display the measured axial ratio and phase difference of the

antennas for different θ_{inc}. The finite size of the FSS limits the angular measurements to

a maximum of $\theta_{inc} = 40°$. The results show that the surface remains CP transparent up to

$\theta_{inc} = 40°$. At higher angles of incidence the bandwidth should decrease due to the

difference between the Floquet modes, shown in Figure 23, will have increased off of

the center frequency. All of these results experimentally show that the surface is

transparent to circular polarization up to $\theta_{inc} = 40°$, and that the chirality of the spiral

does not affect the handedness of the incident wave.

76
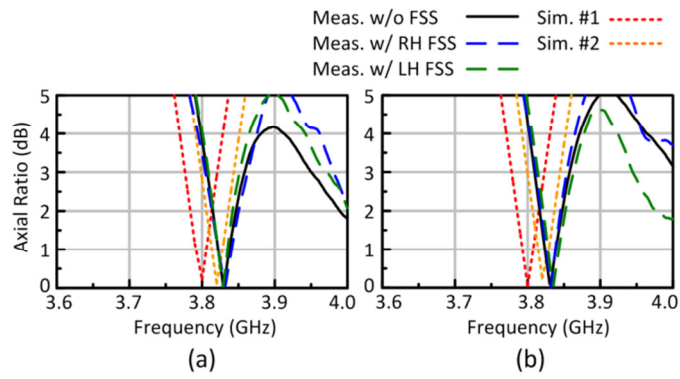
Figure 64 *The axial ratio of the LH (a) and RH (b) antennas in the presence of the FSS.*
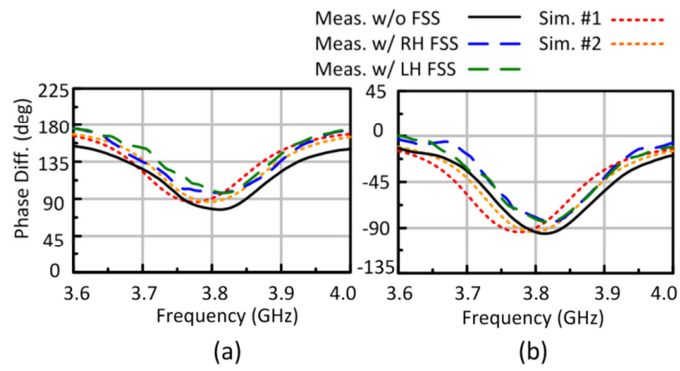
Figure 65 *The phase difference of the LH (a) and RH (b) antennas in the presence of the FSS.*
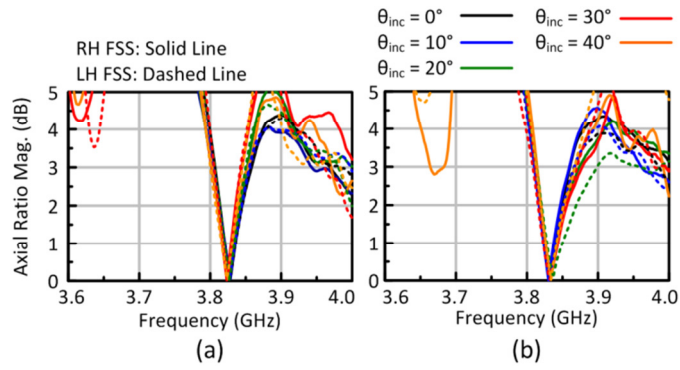
Figure 66 *The measured axial ratio of the LH (a) and RH (b) antennas for different θ_inc.*
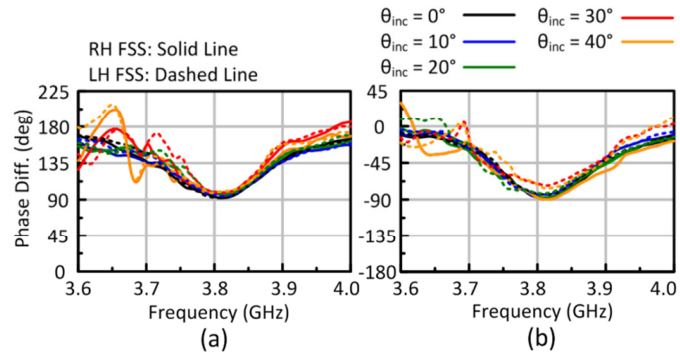
Figure 67 *The measured phase difference of the LH (a) and RH (b) antennas for different θ_inc.*

5. DUAL BAND DESIGNS

5.1.   *Four-arm Dual-band Design*

Two design methods are discussed to create a dual-band FSS by manipulating the spiral's arm lengths. The first method involves putting two four-arm resonators with different arm lengths inside the unit cell. Figure 68 shows the layout of this design. With the addition of the second resonator the unit cell becomes longer in the y-direction with a side length of $2D$. The design parameters for the two spirals are the same as the previous four-arm single-band design except that $N_t = 1.045$ and 1.140. The spiral with the longer arms corresponds to the lower center frequency. The spirals were fabricated on a 1.575 mm Duroid 5880 board through a chemical etching process, and are laid out in a 4 by 8 square grid. It should be noted that the elongation in the y-direction breaks the symmetry between the TE_{00} and TM_{00} modes, but this is a design tradeoff. Figures 68 and 69 show the measured and simulated results. Both surfaces have a lower center frequency, by about 1-2%, than simulation, but all of the results are in close agreement with each other. The circuit model for the dual-band designs will be discussed in the next section. This shift in resonant frequencies can be attributed to the fabrication process. As stated in section 4.2, the chemical etching process is isotropic, and as such there will be a lateral etching component that makes the arms physically and electrically longer that shifts the center frequency down. Overall, the surfaces are in good agreement with the measured results.

79
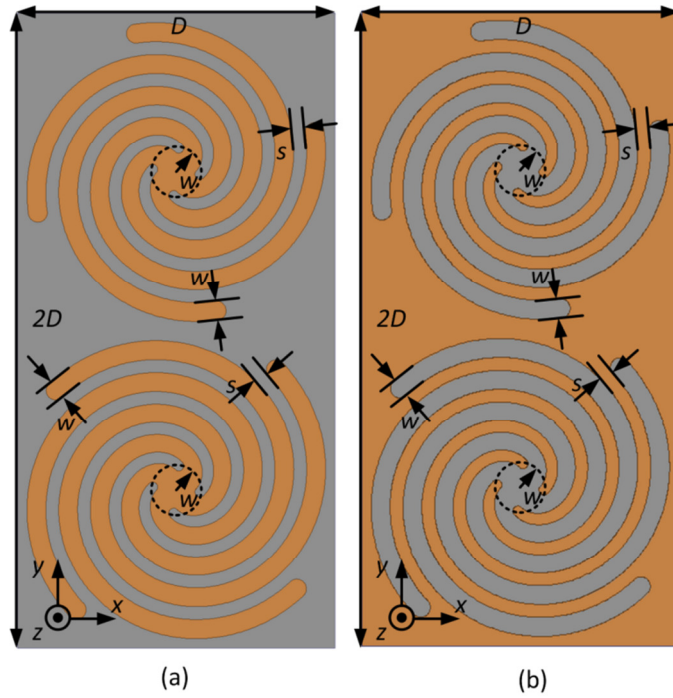
Figure 68 The geometry of the dual-band four-arm metal spiral design (a) and the four-arm slot spiral (b) with alternating element sizes.
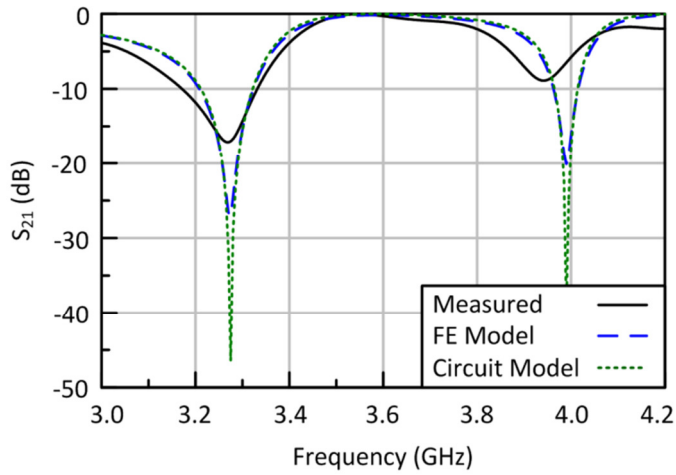
Figure 69 The measured and simulated frequency response of the dual-band four-arm metal spiral.
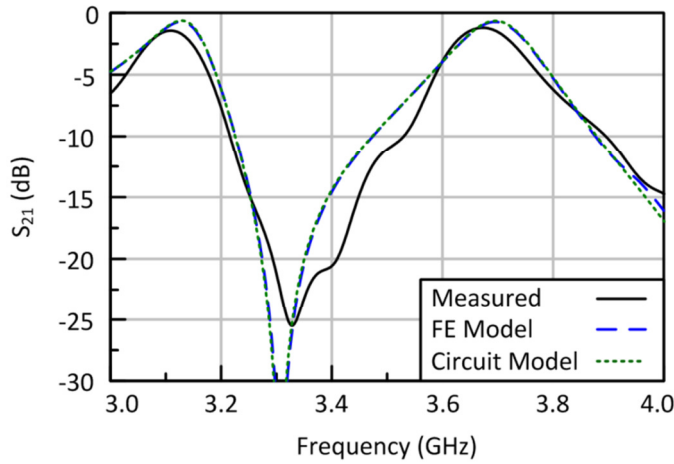
Figure 70 *The measured and simulated frequency response of the dual-band four-arm slot spiral.*

5.2. *Dual-band Eight-arm Design*

This next dual-band method involves taking the two four-arm spirals and superimposing them over each other to create an eight-arm design. Figure 71(a) and (b) show the unit cell design of the metal and slot spirals. The spiral's arms alternate between short and long so that no two arms of the same length are next to each other. To fit an eight-arm FSS inside the waveguide measurement system the spirals had to lie in a 5 by 5 square grid with a unit cell length of $D = 15.72$ mm. The number of turns of the spirals are $N_t = 0.730$ and 0.795. The other design parameters remain unchanged from the previous four-arm design. All of the measured resonant frequencies are lower than the simulated versions, with the largest error being -2.34% for the eight-arm metal spiral's upper stop-band. As stated previously, this error is caused by lateral etching in the fabrication process. Aside from these small frequency shifts, both methods illustrate how to create a dual-band FSS using a multi-arm Archimedean spiral.
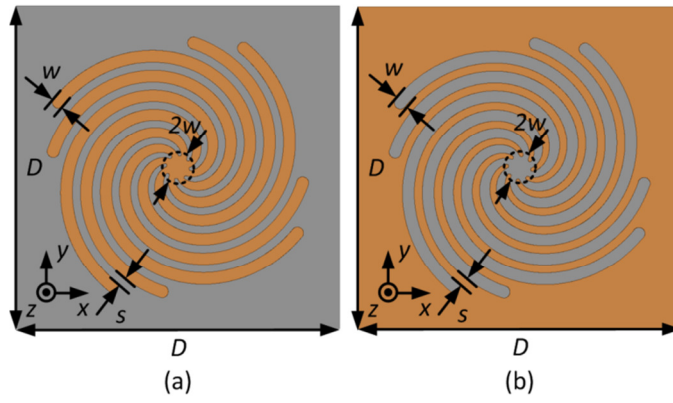
Figure 71 *The geometry of the dual-band eight-arm metal spiral (a) and slot spiral (b).*
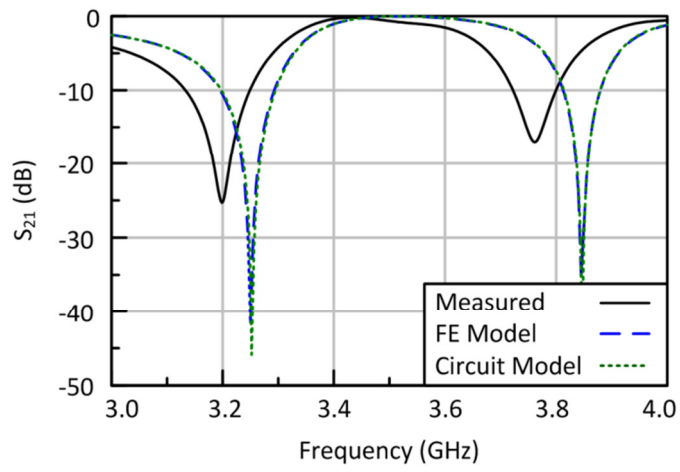
Figure 72 *Measured and simulated results for the dual-band eight-arm metal spiral.*
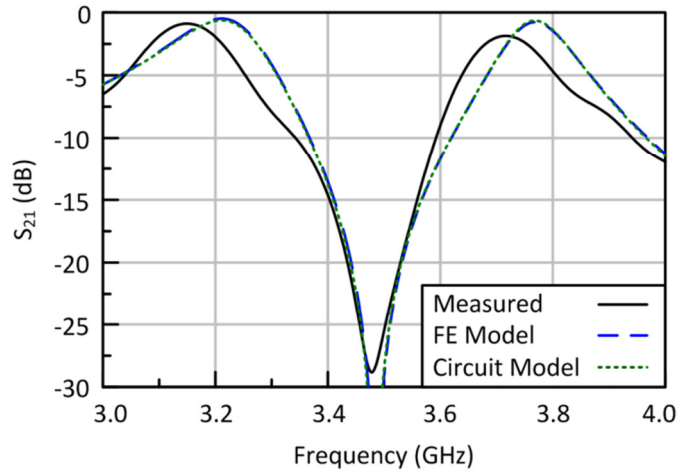
Figure 73 *The measured and simulated frequency response the dual-band eight-arm slot spiral.*

The circuit model for both designs has the same layout. The second resonance is modeled as another RLC set defined by the second set of arc lengths, length extensions, and coupling. The higher order modes are lumped together into a single reactive component representing the dominate reactive component of the next order mode. Table 5 lists the equivalent length extensions, nearest neighbor coupling, and higher order mode terms generated by ADS. The difference between the two models is that all of the fitting parameters are different. All of the circuit model results were in excellent agreement with the FE results.

Table 5 - Optimized Circuit Parameters for the Dual-band Surfaces

FSS Type	Coupling 1	Coupling 2	ΔL_{ext1} (mm)	ΔL_{ext2} (mm)	$X_{Higher\ Order}$
4-arm BS	12.76 fF	28.64 fF	0.166	0.417	51.43 fF
4-arm BP	405.1 pH	420.8 pH	1.20	1.44	1.558 pH
8-arm BS	8.581 fF	32.87 fF	0.0374	0.631	75.22 fF
8-arm BP	326.3 pH	649.4 pH	0.469	0.591	1.135 pH

6. FLUIDIC RECONFIGURATION

6.1.   *Fluidic Channel Design*

To achieve fluidic reconfiguration a superstrate with cylindrical reservoirs attaches to the four-arm designs discussed in section 3. Figure 74 shows the layout of the fluidic unit cell. The superstrate is a hollow cylindrical reservoir that has inlet and outlet channels along the x-axis. This segments the FSS into individual rows. PTFE tubing attaches to the inlet and outlet holes on the perimeter of the finite FSS. Fluid is pumped into the reservoir via a syringe. This setup adds some asymmetry to the system making the TE_{00} and TM_{00} modes non-symmetric. Simulations show that the difference between the modal resonant frequencies is 20 MHz, which is a small, but an unavoidable breaking in symmetry due to addition of the fluidic network. Figure 75 depicts the four-arm metal surface with the superstrate and tubing attached. The design parameters for the fluidic superstrate are the reservoir height c_h = 3.3 mm, reservoir diameter c_d = 9 mm, superstrate height s_h = 6.3 mm, and the inlet/outlet channel diameter i_d = 3.3 mm. This inlet diameter is larger than the 0.5 mm inlet diameter used in [45]. By increasing the diameter the internal pressure will decrease at these junctions and decrease the probability of a channel blow out. An adhesive layer bonds the FSS to the superstrate. When the reservoir is full the dielectric fluid increases the effective capacitance of the spiral which lowers the resonant frequency. The dielectrically loaded resonant frequency and effective dielectric constant are related by

$$f_{loaded} = \frac{f_{air}}{\sqrt{\varepsilon_{reff}}} \qquad (38)$$

with f_{air} being the resonant frequency of the FSS without any dielectrics. Doping the fluid with high dielectric particles creates a variable dielectric constant and thus a tunable resonant frequency.
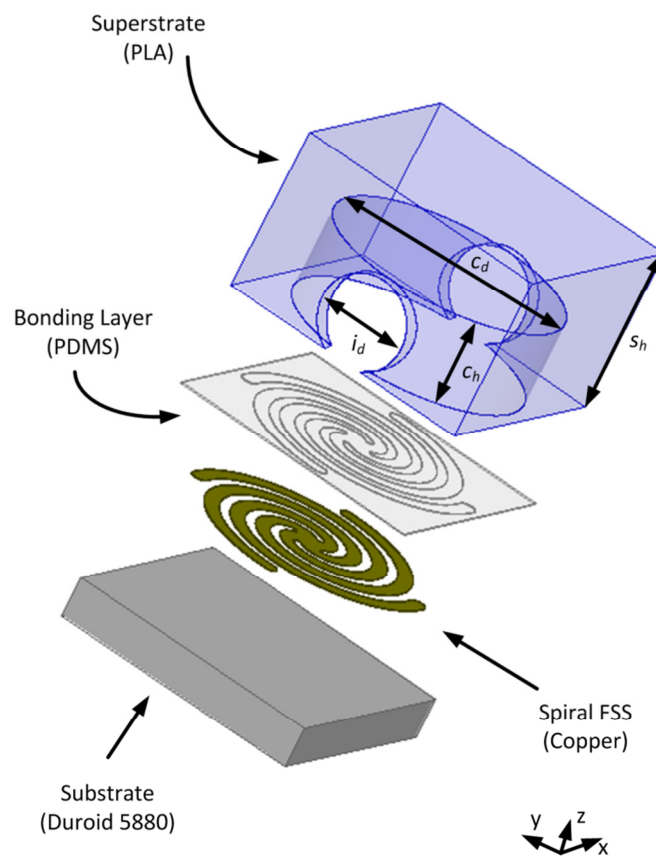
Figure 74 *An expanded view of the FSS and channel layer.*
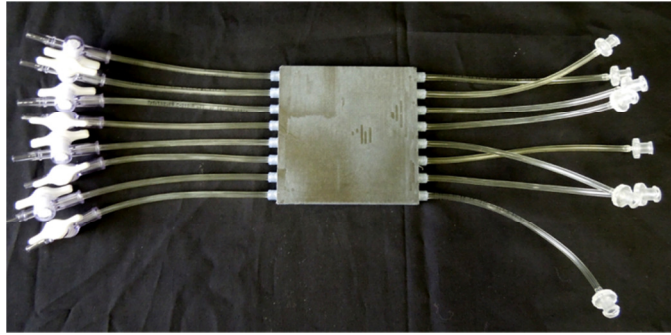
Figure 75 The four-arm metal spiral with the fluidic superstrate. The superstrate is on the bottom. PTFE tubing attaches to the inlet and outlet channels. The ends of the tubing have connectors and valves that enable syringes to attach to the system.

6.2.   Fabrication of the Channel Structure and Bonding Technique

The superstrate layer was printed using polylactic acid (PLA) from the Makerbot Replicator™ 2 desktop 3-D printer. PLA's estimated dielectric properties are $\varepsilon_r = 3.0$ and a $\tan\delta = 0.02$. The color of the PLA is translucent blue. This color was chosen due to the abundance in supply at the initial stage, and its atheistic appeal.

The first round of experiments pumped Fluorinert FC-70, whose dielectric properties are listed in [65], into the reservoirs, and revealed that the PLA superstrate is porous. What indicated this is that several channel segments required more fluid than others to fill up. This was further substantiated by a visual examination of the channel structure. There were various discoloration spots that appeared when the channels were filled. Figure 76(a) illustrates the discoloration caused by Fluorinert FC-70 seeping into the superstrate. The 3-D printer creates the channel structure by laying down crisscrossing lines of heated liquid plastic that solidifies when it cools. Microchannels are created due to the lines of plastic cooling at separate times. Figure 76(b) shows the

87

microchannels in the roof of the reservoir. Fluorinert FC-70 flows into these microchannels, and creates the discoloration. To reduce fluid leaking into the superstrate a thin layer of PDMS, $\varepsilon_r = 2.66$ and $\tan\delta = 0.04$, is coated on the inner surface of the reservoir and left to air dry for 24 hours. After one day the PDMS was viscous enough that it did not drip onto the FSS when it was attached. This layer is thin and immeasurable due to the PDMS being amorphous and filling the micro channels. PDMS has a dielectric constant near that of PLA, which means that the effective dielectric constant of the superstrate doesn't appreciably change. An equally weighted average of the two values yields a 5% decrease in the dielectric value of PLA. This PDMS layer is quite thin and far enough away from the spirals that it is not included in the FE simulations or circuit model due to its negligible impact. The arrangement of the dielectric layers is neither monotonically increasing nor decreasing in dielectric strength. The conformal mapping condition for analytical calculation of the effective dielectric constant is not met. Future work could involve investigation into various material combinations to allow for an analytical solution for the effective dielectric constant. An approximate effective dielectric constant is calculated using a volume average of the materials.
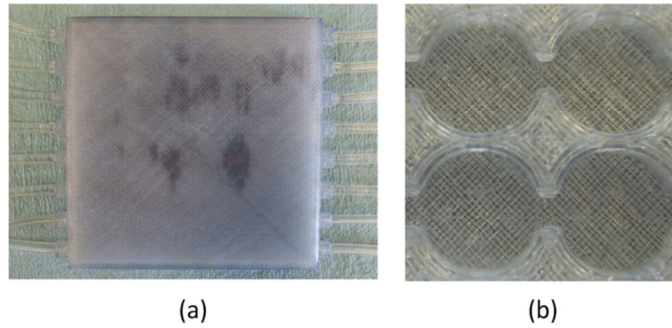
Figure 76 *The PLA made superstrate is porous. The discoloration in the channel network (a) is from Fluorinert FC-70 seeping into the microchannels created by the printing process (b).*

To bond the superstrate to the FSS PDMS is used as the bonding agent. PDMS was chosen as a bonding agent because it is non-toxic, moldable, and the bond is removable. This last property enables multiple uses of the same surface. The PDMS can be removed with the rough side of a sponge without damaging the spirals. The first set of experiments only had the PDMS coating the channel structure in order to bond to the surface leaving the spirals mostly uncovered. During the experiments BSTO particles got caught in the uneven surface of the spirals. To reduce the unevenness a thin layer of PDMS, measured to be about 85μm thick, covered the whole surface and the channels were then attached to it. The assembled structure was air dried. The glass point of PLA is 65°C. PDMS is often heated in an oven to decrease curing time [66]. Placing the assembled structure in the oven at a lower temperature than the glass transition point of PLA resulted in the channel structure uniformly shrinking and no longer fitting on the FSS. The complete structure had to be air dried with the substrate on the bottom, and weight on the top to ensure uniform adhesion. Air curing the PDMS took about 72 hours before it was dry.

6.3.   *Modifications to the Waveguide Measurement System*

The channel layer includes inlet and outlet stubs for the PTFE tubing, which make it unable to fit inside the sample holder. A new sample holder was machined with horizontal channels to allow for the PTFE tubing. Figure 77 depicts the new sample holder. These holes are square with a side length of 6.35 mm. The TE_{10} cutoff frequency is 23.62 GHz. The measurements system operates well below this frequency. However, there needs to be verification that these holes do not significantly perturb the RF fields inside the waveguide.
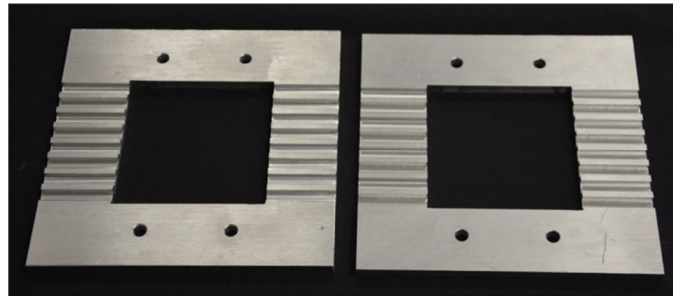
Figure 77 The new sample holder/line standard with horizontal channels to accommodate the fluidic channel structure.

As a quantitative analysis, the S-parameters of both sample holders were measured while empty and attached to the custom waveguide segments. The waveguide is calibrated with a sliding load S-band calibration kit manufactured by Mega Industries. The calibration plane is set between the waveguide launchers and the custom waveguide segments. Figures 78 and 79 show the simulated and measured S_{11} and S_{21} of the samples holders, respectively. All of the measurements and simulations are in close

90

agreement with each other. If the slots reactively loaded the system then the valleys and

peaks in the measured S-parameters would occur at different frequencies for the

different sample holders. These results indicate that the addition of the slots negligibly

perturbs the system.
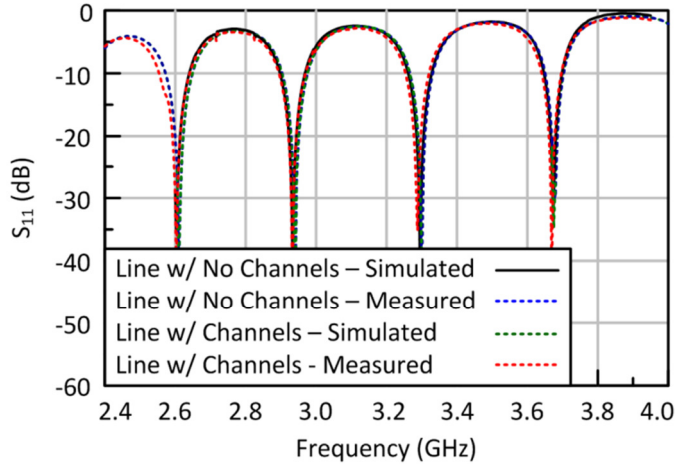
Figure 78 The measured and simulated S$_{11}$ results of the two sample holders.
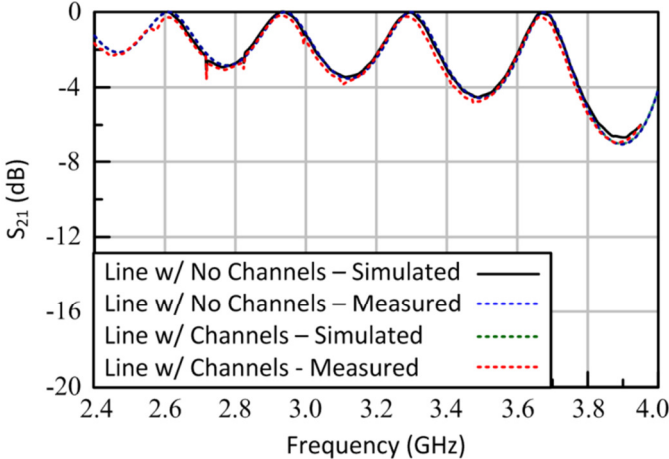
Figure 79 The measured and simulated S$_{21}$ values of the two sample holders.

6.4.   *Background Fluid Investigation*

To create a tunable dielectric, a low dielectric value fluid is doped with high dielectric BSTO particles, $\varepsilon_r = 500$ and $\tan\delta = 0.05$. A design challenge with BSTO particles is that they have a tendency to settle. One solution is to use a more viscous background fluid in order to extend the time that the BSTO particles are suspended. Fluorinert FC-70™ and Hydrocal™ 2400 were chosen as alternatives to silicone oil which was used in [45]. Fluorinert FC-70 is commonly used as a coolant in supercomputers due to its low electrical conductivity. Hydrocal 2400 is a more viscous fluid than Fluorinert FC-70. It is classified as naphthenic oil, and one of its uses is that of an electrical insulator in power transformers. A slim form dielectric probe kit measured the dielectric properties of Hydrocal 2400. Measurements with this kit assume the fluid is isotropic and infinite in extent [67]. This latter assumption requires that probe have a minimum insertion depth of 5 mm from the tip to the surface of the water, and at least 5 mm distance from the base of the fluid's container. For the loss tangent the resolution is only $+/- 0.05|\varepsilon_r*|$. Hydrocal 2400 had a median $\varepsilon_r = 2.35$ and an estimated median $\tan\delta = 0.035$, which is small compared to the dielectric constant of BSTO.

To test the usability of the fluids as a dispersion, a 10% volume fraction of BSTO particles was added to the fluids and stirred for 5 minutes. Glass beakers and a glass stirring rod were used. With the Fluorinert FC-70 mixture, once stirring ceased the particles immediately started to settle on the bottom of the beaker. After about a minute there was significant particle collection at the bottom of the beaker and visual inspection of the fluid showed that it was no longer uniformly mixed. When BSTO was mixed with

Hydrocal 2400 the particles took longer to settle. After 10 minutes the mixture had a uniform creamy yellow hue to it with minimal settling on the bottom. After 25 minutes there was a noticeable white ring on the bottom, and after 50 minutes there was significant settling on the bottom with the mixture having a more pronounced yellow tint to it, which indicates that there were less BSTO particles in the upper part of the mixture. Figure 80 shows a beaker will Hydrocal 2400 doped with a 10% BSTO volume fraction after 50 minutes. The white ring on the bottom is an accumulation of BSTO particles that have settled. This empirical observation reveals that a Hydrocal 2400 mixture has about a 10 minute usability time span starting from the time that stirring ceased. Due to the BSTO particles staying suspended in Hydrocal 2400 longer than Fluorinert FC-70, Hydrocal 2400 is the more appropriate choice for creating a tunable dielectric fluid using BSTO particles.

Both Fluorinert FC-70 and Hydrocal 2400 were flowed through the channel structure. Figure 81 shows the magnitude frequency response of the four-arm metal spiral with air, Fluorinert FC-70 and Hydrocal 2400 filling the reservoirs. Figure 82 shows the magnitude frequency response for the four-arm slot spiral with the same materials filling the reservoirs. In both cases the Fluorinert FC-70 and Hydrocal 2400 measurements are in good agreement with the FE results – except for the air case. However, the circuit model disagrees with both the measured results and the FE results.

Figure 80 Hydrocal 2400 doped with BSTO particles after 50 minutes. The white ring at the bottom of the beaker is from BSTO particles that have settled.

The discrepancy in the air case is most likely caused an increase in PDMS thickness over the spirals from the fabrication process. During fabrication PDMS is coats the entire surface, and when the channel structure is attached it is mechanically pressed into place. This compression displaces some PDMS and forces it partially over the spirals. Also, from the published product sheet [66] it takes PDMS about 48 hours to cure. For these experiments it took the PDMS about 72 hours to fully cure, but this was limited to visual inspection on the outside of the FSS. Besides disassembling the FSS and superstrate there is no way to tell how cured the PDMS is on the inside of the FSS. When the background fluids flow through the channels it could either dilute the uncured

94

PDMS or push it off of the spirals, which could explain why the FE results for Fluorinert FC-70 and Hydrocal 2400 are in better agreement with the measured results. In addition to this discrepancy in center frequencies, the insertion loss for the slot spiral design is larger than predicted. This indicates that losses are larger than predicted. The loss tangents of the fluids and PLA were estimated, and the losses due to surface waves were assumed to be negligible. In comparison to the experiments in [45], the stop-band experiments maintained a sufficient level of suppression, and the channels did not leak.
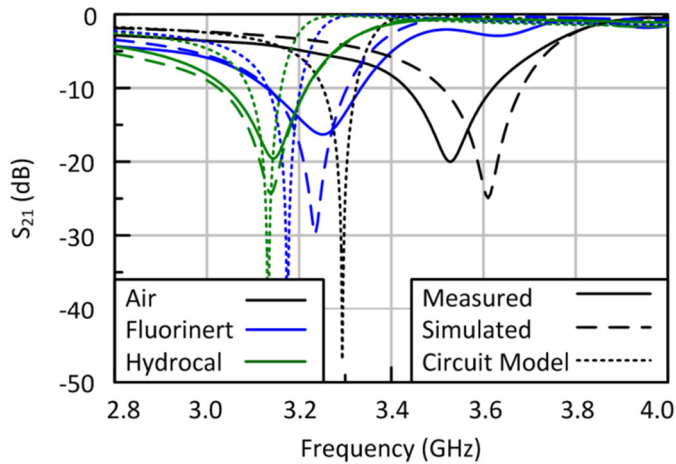
Figure 81 *Measured and simulated results for the metal spiral fluidic system when different low dielectric fluids are present in the channels.*
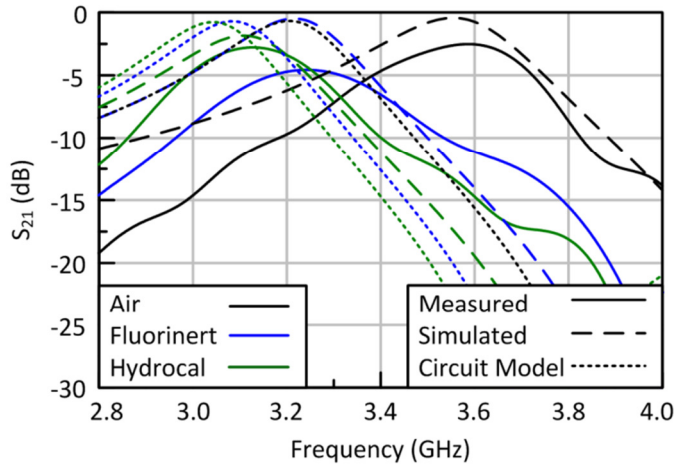
Figure 82 The measured and simulated results for the slot spiral fluidic system when different low dielectric fluids are present in the channels.

6.5.   Dynamic Tuning Experimental Results

Figures 83 and 84 show the results for the fluidic tuning experiment performed on the FSS. Measurements and FE simulations are in close agreement for a zero volume fraction, but they begin to diverge as the volume fraction is increased. The circuit model disagrees for all cases. This disagreement is due to the volume average of the effective dielectric constant not being an accurate representation. The divergence between the measured results and FE model is caused by particles settling on the surface and sticking to the channel walls as depicted in Figure 85. One method for decreasing particle settling on the surface would be to use a thinner layer of copper, which would decrease the surface roughness and areas where particles would become trapped. The internal settling causes an increase in volume fraction of the material and decreases the resonant frequency further than predicted as seen in the 20% and 30% volume fraction curves. The slot spiral design was more susceptible to this settling in that the pass-band suffered

96

a significant increase in the insertion loss. Leaks at the outer channel wall became more frequent with higher volume fractions. Due to the increase in viscosity of the liquid for higher volume fractions it required more force to move the liquid thus increasing internal pressure, and the probability of a channel leak forming increased. The upper limit for mechanical stability was for volume fractions of 30%. This was a significant improvement in mechanical stability versus the system in [45].
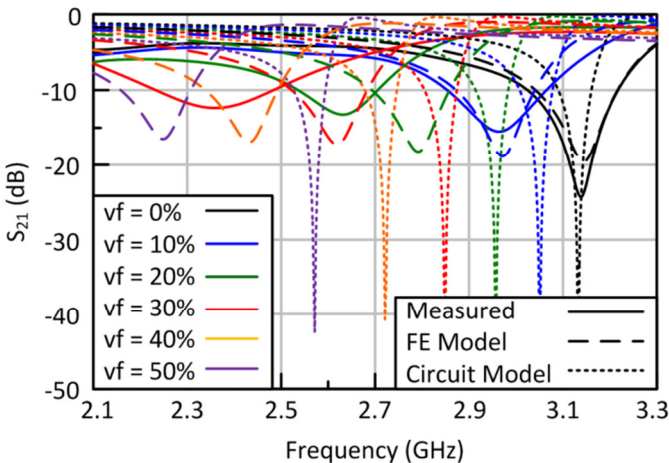
Figure 83 *Fluidic tuning of the four-arm metal spiral FSS.*
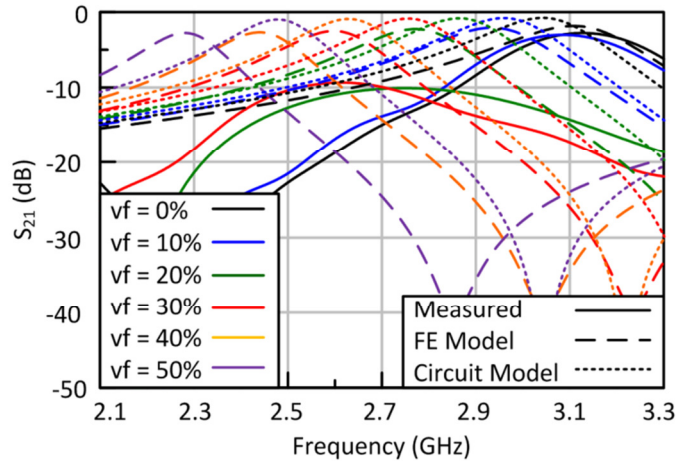
Figure 84 *Fluidic tuning of the four-arm slot spiral FSS.*
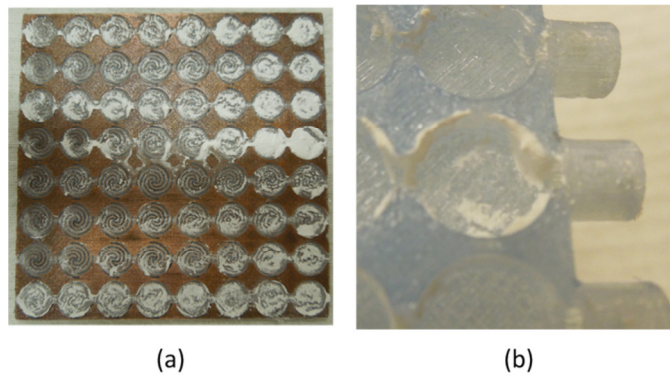
Figure 85 *The BSTO particles settled on the surface inside the copper traces (a), and stuck to the channel walls (b).*

These fluidic experiments provide an alternative channel design to the one presented in [45]. This version tunes the whole surface instead of a couple resonators. The channel structure was more stable for lower volume fractions, but the failure rate increased when using 30% BSTO volume fractions. This design illustrates how manipulation of a fluid's dielectric properties tunes the resonant frequency of a frequency selective surface. However, the material properties prevent an analytical

98

model of the effective dielectric constant. A possible research path would be to

investigate various material combinations that would allow for a predictive model of the

effective dielectric constant, and facilitate a more stable tunable dielectric mixture.

7. CONCLUSIONS AND FUTURE WORK

This work presented an analysis of multi-arm Archimedean spirals, and illustrated a method for fluidic reconfiguration. Archimedean spirals provide a mathematically defined geometric alternative for electrically small resonators in a FSS. Examination of simulations involving various spiral designs reveal that the arms behave similar to periodic coplanar transmission line resonators. Their arms are about a quarter wavelength long. However, simulations show that single-arm spirals behave differently. Adding additional arms to the spiral is akin to adding degenerate poles and zero to a filter, but with the caveat of the added arms increasing the electrical size of the spiral.

The lattice structure and number of arms affects the frequency response of the TE and TM modes. For the one- and two-arm designs the modes are dependent on the orientation of the spiral in the x-y plane. Simulations show that when these spirals are rotated 90° the TE and TM modes swap behavior. The three-arm spiral has near modal symmetry with a simulated difference between modes of about 15 MHz. The four- and eight-arm spirals have complete modal symmetry when in a square lattice. The four-arm spiral kept its modal symmetry when placed in a triangular lattice with a slant angle of Ω = 60°. However, the modal symmetry breaks when a tightly packed four-arm spiral rests in a hexagonal lattice. When a six-arm spiral was placed inside the hexagonal lattice the modal symmetry returned. These simulations showed that the lattice and resonator geometry have to have the same axis of symmetry for there to be modal symmetry.

100

With the TE_{00} and TM_{00} modes being the same for the four-arm spiral in a square lattice it is implied that the surface would be transparent to circular polarization. LH and RH patch antennas were used to test the CP transparency of the surface. Results showed that for angles up to $\theta_{inc} = 40°$ the surface remains transparent to circular polarization. In addition, experimental results show that the chirality of the spiral does not affect the handedness of the incoming wave. One application space where this property would be useful is satellite communication where CP is preferred.

Dual-band surfaces were created by manipulating the arm lengths of the spiral. Two methods were discussed. The first method added a second spiral, with a longer arm length, to the unit cell of the four-arm design. This elongates the unit cell in one direction, and breaks modal symmetry. The second method superimposes the two four-arm spirals over each other and creates a single eight-arm spiral with a dual-band frequency response. Measurements of both designs are in good agreement with the simulated results. These methods illustrate how to create a dual-band FSS through manipulation of the spiral's natural shape instead of adding an elaborate tuning mechanism to the structure.

Two low loss dielectric fluids were investigated as alternatives to silicone oil. The low viscosity fluid Fluorinert FC-70 did not suspend the BSTO particles long enough for the mixture to be used in the reconfiguration experiment. The other fluid Hydrocal 2400 suspended the particles for about 10 minutes before the settling. More research into various fluid and particle combinations for use in RF applications is

required. A good line of inquiry would be to investigate low loss fluids that have immiscible particle counterparts that would create a stable tunable fluidic mixture.

The updated channel structure presented in this work showed an improvement in mechanical stability compared to [45]. Instead of having narrow channels come from beneath the surface the inlet and outlet channels in this work's channel layer were horizontal across the surface. There were reservoirs above all of the spirals instead of just the center 16. The whole surface was tuned. With the channel structure attaching to the surface in a specific orientation the placement issues observed in the static experiments were not present. In addition, all of the metal spirals retained a sufficient level of suppression to remain classified as a band-stop filter. Experimental results for the slot spiral showed similar tuning of the pass-band. However, the insertion loss for higher volume fractions significantly attenuated the pass-band. For a volume fraction of 30% the pass-band of the slot spiral was below -10 dB. Being able to use up to a 30% volume fraction is a significant improvement in the tuning range compared to a limit of 10% observed in [45]. Overall, this new channel design displayed several improvements over the previous iterations.

The fluidic dispersion experiments demonstrated frequency tuning, but there was disagreement between the FE simulations, circuit model, and measured results. The center frequencies of all three differ for higher volume fractions. The experimental results differed because there was particle settling on the chamber walls and on the surface itself. The additional particles increased the effective dielectric constant of the superstrate and shifted the center frequency lower than simulations predicted. For future

102

experiments a way to reduce this would be to decrease the copper thickness of the spiral traces in order to minimize any surface roughness. Also, the channel walls inside the 3-D printed superstrate needs to be smooth in order to reduce the areas where particle can catch as well as elimination of the microchannels. Investigation into different 3-D printing methods could enable better fluid flow and elimination of the microchannels.

The disagreement with the circuit model was the result of taking a volume average of the effective dielectric constant. This method assumed an equal weighting to the dielectric constants of the materials. As simulations and theory showed the center frequency approaches an asymptotic value for relatively thin substrates. This indicates that the first few layers of a stratified layer will have more of an effect than the later ones. Any bonding material would need to be included in the simulation no matter how thin. In addition, calculation of the effective dielectric constant using conformal mapping has the requirement that subsequent layers must be monotonically increasing or decreasing in their dielectric strength. The dielectric layers in these experiments are not monotonically increase or decreasing. A possible area of research would be to make the theoretical method more general so as to allow for random dielectric layers. An improvement in the theoretical calculation would make the circuit model more accurate.

A multi-arm Archimedean spiral has several beneficial properties. It's electrically small, certain geometries have angular frequency stability and modal symmetry, its center frequency is a function of its arm length, and its four-arm slot spiral geometry is transparent to a CP plane wave. Fluidic reconfiguration can be achieved using this geometry, but it may not be the optimal geometry for fluidic reconfiguration.

Other geometries, such as a dipole slot, might be better suited because they are not as greatly influenced by thin dielectric layers like the spiral. Fluidic tuning of FSSs is possible, but further material research is required.

REFERENCES

[1]   Ansys, "Getting Started with HFSS Floquet Ports," ed: ANSYS, Inc., 2012, p. 72.

[2]   B. Munk, *Frequency selective surfaces : theory and design*. New York: John Wiley, 2000.

[3]   R. Marqués, J. D. Baena, M. Beruete, F. Falcone, T. Lopetegi, M. Sorolla*, et al.*, "Ab initio analysis of frequency selective surfaces based on conventional and complementary split ring resonators," *Journal of Optics A: Pure and Applied Optics,* vol. 7, p. S38, 2005.

[4]   E. A. Parker and A. N. A. El Sheikh, "Convoluted dipole array elements," *Electronics Letters,* vol. 27, pp. 322-323, 1991.

[5]   E. A. Parker, A. N. A. El-Sheikh, and A. C. d. Lima, "Convoluted frequency-selective array elements derived from linear and crossed dipoles," *Microwaves, Antennas and Propagation, IEE Proceedings H,* vol. 140, pp. 378-380, 1993.

[6]   Y. Li-Hua, W. Zheng-Fei, Z. Zhi-Yuan, W. Wen, and F. Da-Gang, "A miniaturized frequency selective surface based on convoluted ring slot," in *Environmental Electromagnetics (CEEM), 2012 6th Asia-Pacific Conference on*, 2012, pp. 63-66.

[7]   E. A. Parker, J. C. Batchelor, R. Chiang, A. G. Williamson, B. Sanz-Izquierdo, M. J. Neve*, et al.*, "Frequency selectively screened office incorporating convoluted FSS window," *Electronics Letters,* vol. 46, pp. 317-318, 2010.

[8]   N. Behdad, "Miniaturized-element frequency selective surfaces (MEFSS) using sub-wavelength periodic structures," in *Radio and Wireless Symposium, 2008 IEEE*, 2008, pp. 347-350.

[9]   N. Behdad and K. Sarabandi, "A miniaturized band-pass frequency selective surface," in *Antennas and Propagation Society International Symposium 2006, IEEE*, 2006, pp. 4171-4174.

[10]   K. Sarabandi and N. Behdad, "A frequency selective surface with miniaturized elements," *Antennas and Propagation, IEEE Transactions on,* vol. 55, pp. 1239-1245, 2007.

[11]   J. Kaiser, "The Archimedean two-wire spiral antenna," *Antennas and Propagation, IRE Transactions on,* vol. 8, pp. 312-323, 1960.

[12]   C. Teng-Kai and G. H. Huff, "On the constant input impedance of the Archimedean spiral antenna in free-space," *Antennas and Propagation, IEEE Transactions on,* vol. 62, pp. 3869-3872, 2014.

[13]   P. C. Werntz and W. L. Stutzman, "Design, analysis and construction of an Archimedean spiral antenna and feed structure," in *Southeastcon '89. Proceedings. Energy and Information Technologies in the Southeast., IEEE*, 1989, pp. 308-313 vol.1.

[14]   L. Wanlu, Y. Guohui, Z. Tong, W. Qun, H. Jun, C. Meiliang*, et al.*, "A novel miniaturized band-pass frequency selective surface," in *Millimeter Waves (GSMM), 2012 5th Global Symposium on*, 2012, pp. 245-248.

[15]   P. Callaghan and E. A. Parker, "Experimental investigation of closely packed spiral element FSS yields narrowband designs," in *Antennas and Propagation, 1991. ICAP 91., Seventh International Conference on (IEE)*, 1991, pp. 636-639 vol. 2.

[16]   D. K. Wickenden, R. S. Awadallah, P. A. Vichot, B. M. Brawley, E. A. Richards, J. W. M. Spicer*, et al.*, "Polarization properties of frequency-selective surfaces comprised of spiral resonators," *Antennas and Propagation, IEEE Transactions on,* vol. 55, pp. 2591-2597, 2007.

[17]   L. D.-C. Tzuang, J. Yu-Wei, Y.-H. Ye, Y.-T. Chang, Y.-T. Wu, and S.-C. Lee, "Polarization rotation of shape resonance in Archimedean spiral slots," *Applied Physics Letters,* vol. 94, pp. 091912-091912-3, 2009.

[18]   W. Te-Kao and L. Shung-Wu, "Multiband frequency selective surface with multiring patch elements," *Antennas and Propagation, IEEE Transactions on,* vol. 42, pp. 1484-1490, 1994.

[19]   C. A. Balanis, *Modern antenna handbook*. Hoboken, NJ: Wiley, 2008.

[20]   A. Bhattacharyya, *Phased array antennas : Floquet analysis, synthesis, BFNs, and active array systems*. Hoboken, N.J.: Wiley-Interscience, 2006.

[21]   T. K. Wu, *Frequency selective surface and grid array*. New York: Wiley, 1995.

[22]   F. Bayatpur and K. Sarabandi, "Design and analysis of a tunable miniaturized-element frequency-selective surface without bias network," *Antennas and Propagation, IEEE Transactions on,* vol. 58, pp. 1214-1219, 2010.

[23]   C. Mias, "Varactor tunable frequency selective absorber," *Electronics Letters,* vol. 39, pp. 1060-1062, 2003.

[24]   C. Mias, "Varactor-tunable frequency selective surface with resistive-lumped-element biasing grids," *Microwave and Wireless Components Letters, IEEE,* vol. 15, pp. 570-572, 2005.

[25]   A. Munir, V. Fusco, and O. Malyuskin, "Tunable frequency selective surfaces characterisation," in *Microwave Conference, 2008. EuMC 2008. 38th European*, 2008, pp. 813-816.

[26]   B. Sanz-Izquierdo and E. A. Parker, "Dual polarized reconfigurable frequency selective surfaces," *Antennas and Propagation, IEEE Transactions on,* vol. 62, pp. 764-771, 2014.

[27]   G. M. Coutts, R. R. Mansour, and S. K. Chaudhuri, "A MEMS-tunable frequency-selective surface monolithically integrated on a flexible substrate," in *Microwave Symposium, 2007. IEEE/MTT-S International*, 2007, pp. 497-500.

[28]   T. K. Chang, R. J. Langley, and E. A. Parker, "Frequency selective surfaces on biased ferrite substrates," *Electronics Letters,* vol. 30, pp. 1193-1194, 1994.

[29]   P. S. Taylor, J. C. Batchelor, and E. A. Parker, "A passively switched dual-band FSS slot array," in *Antennas and Propagation (EUCAP), Proceedings of the 5th European Conference on*, 2011, pp. 507-510.

[30]   P. S. Taylor, J. C. Bathelor, and E. A. Parker, "A passively switched dual-band circular FSS slot array," in *Antennas and Propagation in Wireless*

Communications (APWC), 2011 IEEE-APS Topical Conference on, 2011, pp. 648-651.

[31]   L. Bao Jun, A. Zamora, T. F. Chun, A. T. Ohta, and W. A. Shiroma, "A wideband, pressure-driven, liquid-tunable frequency selective surface," *Microwave and Wireless Components Letters, IEEE,* vol. 21, pp. 465-467, 2011.

[32]   L. Meng and N. Behdad, "Fluidically tunable frequency selective/phase shifting surfaces for high-power microwave applications," *Antennas and Propagation, IEEE Transactions on,* vol. 60, pp. 2748-2759, 2012.

[33]   L. Meng, Y. Bin, and N. Behdad, "Liquid-tunable frequency selective surfaces," *Microwave and Wireless Components Letters, IEEE,* vol. 20, pp. 423-425, 2010.

[34]   A. C. d. Lima, E. A. Parker, and R. J. Langley, "Tunable frequency selective surface using liquid substrates," *Electronics Letters,* vol. 30, pp. 281-282, 1994.

[35]   S. Monni, G. Gerini, and A. Neto, "Frequency selective surfaces for the RCS reduction of low frequency antennas," in *Antennas and Propagation, 2006. EuCAP 2006. First European Conference on*, 2006, pp. 1-6.

[36]   A. Abbaspour-Tamijani, K. Sarabandi, and G. M. Rebeiz, "A planar filter-lens array for millimeter-wave applications," in *Antennas and Propagation Society International Symposium, 2004. IEEE*, 2004, pp. 675-678 Vol.1.

[37]   V. Agrawal and W. A. Imbriale, "Design of a dichroic Cassegrain subreflector," *Antennas and Propagation, IEEE Transactions on,* vol. 27, pp. 466-473, 1979.

[38]   J. C. Batchelor, E. A. Parker, B. Sanz-Izquierdo, J. B. Robertson, I. T. Ekpo, and A. G. Williamson, "Designing FSS for wireless propagation control within

buildings," in *Antennas & Propagation Conference, 2009. LAPC 2009. Loughborough*, 2009, pp. 14-17.

[39] T. Parker, J. Batchelor, J. B. Robertson, B. Sanz-Izquierdo, and I. Ekpo, "Frequency selective surfaces for long wavelength use in buildings," in *Electromagnetic Propagation in Structures and Buildings, 2008 IET Seminar on*, 2008, pp. 1-22.

[40] M. Raspopoulos and S. Stavrou, "Frequency selective buildings through frequency selective surfaces," *Antennas and Propagation, IEEE Transactions on,* vol. 59, pp. 2998-3005, 2011.

[41] J. Roberts, J. M. Rigelsford, and K. L. Ford, "Diffraction from frequency selective surfaces for secure building applications," in *Antennas and Propagation (EUCAP), 2012 6th European Conference on*, 2012, pp. 2388-2391.

[42] Z. Hang, S. Qu, L. Baoqin, J. Wang, H. Ma, X. Zhuo*, et al.*, "Filter-antenna consisting of conical FSS radome and monopole antenna," *Antennas and Propagation, IEEE Transactions on,* vol. 60, pp. 3040-3045, 2012.

[43] F. Bayatpur and K. Sarabandi, "Miniaturized FSS and patch antenna array coupling for angle-independent, high-order spatial filtering," *Microwave and Wireless Components Letters, IEEE,* vol. 20, pp. 79-81, 2010.

[44] Z. Jun and X. Xiaowen, "Study of the effect of a finite FSS radome on a horn antenna," in *Microwave Technology & Computational Electromagnetics (ICMTCE), 2011 IEEE International Conference on*, 2011, pp. 74-76.

[45]   E. C. Wells, "Fluidic Tuning of a four-arm spiral-based frequency selective surface," Master of Science Thesis, Electrical and Computer Engineering, Texas A&M University, 2011.

[46]   S. J. Orfanidis. (2014). *Electromagnetic Waves and Antennas*. Available: http://eceweb1.rutgers.edu/~orfanidi/ewa/

[47]   A. H. Sihvola and Institution of Electrical Engineers., *Electromagnetic mixing formulas and applications*. London: Institution of Electrical Engineers, 1999.

[48]   H. Nakano, J. Yamauchi, and S. Hashimoto, "Numerical analysis of 4-arm Archimedean spiral antenna," *Electronics Letters,* vol. 19, pp. 78-80, 1983.

[49]   H. G. Booker, "Slot aerials and their relation to complementary wire aerials (Babinet's principle)," *Electrical Engineers - Part IIIA: Radiolocation, Journal of the Institution of,* vol. 93, pp. 620-626, 1946.

[50]   T. K. Chen and G. H. Huff, "Analytical investigation of periodic coplanar waveguides," *Progress In Electromagnetic Research M,* vol. 30, pp. 167-181, 2013.

[51]   P. Silvester and P. Benedek, "Equivalent capacitances of microstrip open circuits," *Microwave Theory and Techniques, IEEE Transactions on,* vol. 20, pp. 511-516, 1972.

[52]   W. J. Getsinger, "End-effects in quasi-TEM transmission lines," *Microwave Theory and Techniques, IEEE Transactions on,* vol. 41, pp. 666-672, 1993.

[53]   E. O. Hammerstad, "Equations for microstrip circuit design," in *Microwave Conference, 1975. 5th European*, 1975, pp. 268-272.

[54] R. M. Foster, "A reactance theorem," *Bell System Technical Journal, The,* vol. 3, pp. 259-267, 1924.

[55] P. Callaghan, E. A. Parker, and R. J. Langley, "Influence of supporting dielectric layers on the transmission properties of frequency selective surfaces," *Microwaves, Antennas and Propagation, IEE Proceedings H,* vol. 138, pp. 448-454, 1991.

[56] R. J. Luebbers and B. A. Munk, "Some effects of dielectric loading on periodic slot arrays," *Antennas and Propagation, IEEE Transactions on,* vol. 26, pp. 536-542, 1978.

[57] P. Callaghan and E. A. Parker, "Element dependency in dielectric tuning of frequency selective surfaces," *Electronics Letters,* vol. 28, pp. 42-44, 1992.

[58] D. M. Pozar, *Microwave engineering*, 4th ed. Hoboken, NJ: Wiley, 2012.

[59] R. E. Collin, *Foundations for microwave engineering*, 2nd ed. New York: IEEE Press, 2001.

[60] K. C. Gupta, R. Garg, and I. J. Bahl, *Microstrip lines and slotlines*. Dedham, Mass.: Artech House, 1979.

[61] P. W. Hannan and M. A. Balfour, "Simulation of a phased-array antenna in waveguide," *Antennas and Propagation, IEEE Transactions on,* vol. 13, pp. 342-353, 1965.

[62] F. Bayatpur and K. Sarabandi, "Tuning performance of metamaterial-based frequency selective surfaces," *Antennas and Propagation, IEEE Transactions on,* vol. 57, pp. 590-592, 2009.

[63]   S. A. Campbell, *Fabrication engineering at the micro- and nanoscale*, Fourth

        edition. ed. New York: Oxford University Press, 2013.

[64]   K. R. Carver and J. Mink, "Microstrip antenna technology," *Antennas and

        Propagation, IEEE Transactions on,* vol. 29, pp. 2-24, 1981.

[65]   3M, "Fluorinert electronic liqud FC-70 - product information," ed: 3M, 2000, p.

        4.

[66]   "Information about dow corning brand silicone encapsulants," ed: Dow Corning,

        2005, p. 8.

[67]   "Agilent 85070E dielectric probe kit 200 MHz to 50 GHz - technical overview,"

        ed: Agilent Technologies, 2013, p. 12.